

EVolSplat4D: Efficient Volume-based Gaussian Splatting for 4D Urban Scene Synthesis

Sheng Miao · Sijin Li · Pan Wang · Dongfeng Bai · Bingbing Liu · Yue Wang · Andreas Geiger · Yiyi Liao✉

the date of receipt and acceptance should be inserted later

Abstract Novel view synthesis (NVS) of static and dynamic urban scenes is essential for autonomous driving simulation, yet existing methods often struggle to balance reconstruction time with quality. While state-of-the-art neural radiance fields and 3D Gaussian Splatting approaches achieve photorealism, they often rely on time-consuming per-scene optimization. Conversely, emerging feed-forward methods frequently adopt per-pixel Gaussian representations, which lead to 3D inconsistencies when aggregating multi-view predictions in complex, dynamic environments. We propose EvolSplat4D, a feed-forward framework that moves beyond existing per-pixel paradigms by unifying volume-based and pixel-based Gaussian prediction across three specialized branches. For close-range static regions, we predict consistent geometry of 3D Gaussians over multiple frames directly from a 3D feature volume, complemented by a semantically-enhanced image-based rendering module for predicting their appearance. For dynamic actors, we utilize object-centric canonical spaces and a motion-adjusted rendering module to aggregate temporal features, ensuring stable 4D reconstruction despite noisy motion priors. Far-Field scenery is handled by an efficient per-pixel Gaussian branch to ensure

Yiyi Liao (✉)
E-mail: yiyi.liao@zju.edu.cn

Sheng Miao
E-mail: shengmiao@zju.edu.cn

S. Miao, S. Li, Y. Wang, Y. Liao
Zhejiang University, China.

P. Wang, D. Bai, B. Liu
Huawei, China.

A. Geiger
University of Tübingen, Germany.

Project Page: <https://xdimlab.github.io/EVolsplat4D/>

full-scene coverage. Experimental results on the KITTI-360, KITTI, Waymo, and PandaSet datasets show that EvolSplat4D reconstructs both static and dynamic environments with superior accuracy and consistency, outperforming both per-scene optimization and state-of-the-art feed-forward baselines.

Keywords Gaussian Splatting · 4D Reconstruction · Feed-Forward Reconstruction · Autonomous Driving

1 Introduction

Novel view synthesis (NVS) and scene reconstruction are central to autonomous driving simulation, where photo-realistic and geometrically accurate digital twins of real-world environments at scale are required for training and evaluating autonomous driving algorithms across diverse scenarios. Building on the recent progress in neural radiance fields (NeRF) [Mildenhall et al \(2021\)](#) and 3D Gaussian Splatting (3DGS) [Kerbl et al \(2023\)](#), several works [Rematas et al \(2022\)](#); [Yang et al \(2023b\)](#); [Wang et al \(2023\)](#); [Ye et al \(2024a\)](#); [Kerbl et al \(2024\)](#) have achieved promising NVS performance for urban street scenes. However, all these approaches rely on per-scene optimization, which becomes prohibitively time-consuming when scaling to a large number of urban environments for large-scale simulation.

To remedy this issue, feed-forward methods aim to regress scene representations in a single forward pass. Early approaches learn generalizable NeRFs [Xu et al \(2023\)](#); [Miao et al \(2024\)](#); [Chen et al \(2021\)](#) from input images, but suffer from slow inference due to expensive volumetric sampling. To enable real-time rendering, recent works instead regress 3D Gaussians directly. These methods share a similar design, using 2D CNN and transformer architectures to predict *pixel-aligned* 3D

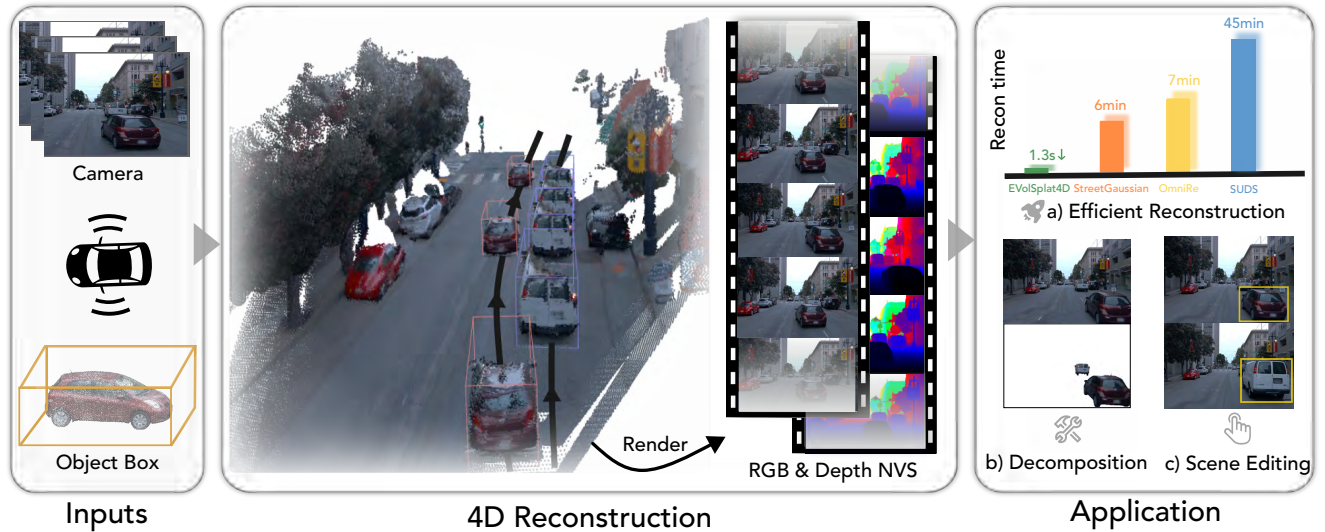


Fig. 1: **Overview of EVolSplat4D.** We propose EVolSplat4D, a unified feed-forward 3D Gaussian Splatting framework tailored for static & dynamic urban scenes that achieves real-time rendering speeds. Leveraging both camera and tracked 3D bounding box as inputs, EVolSplat4D completes scene reconstruction in approximately 1.3 seconds, achieving photo-realistic quality comparable to time-consuming per-scene optimization methods. EVolSplat4D also supports various downstream applications, including high-fidelity scene editing and scene decomposition.

Gaussians from 2D reference images Szymanowicz et al (2024b); Charatan et al (2024); Chen et al (2024b); Xu et al (2025). Although effective for efficient reconstruction and real-time, high-quality NVS in static scenes, these approaches do not directly generalize to dynamic driving scenarios. Recently, pioneering works such as DrivingRecon Lu et al (2024) and STORM Yang et al (2024a) extend pixel-aligned designs to dynamic street reconstruction. However, they still rely on *per-pixel* 3D Gaussian representations, which can easily lead to 3D inconsistencies (e.g., multi-layer artifacts) when a target view aggregates 3D Gaussian predictions from multi-view neighboring viewpoints. The issue is further intensified for dynamic objects, where accurate aggregation additionally depends on precise 3D motion estimation. Moreover, the number of 3D Gaussians scales linearly with the number of 2D pixels, leading to high memory cost and redundant primitives in overlapping regions.

In this paper, we investigate a key question in feed-forward scene reconstruction: is per-pixel prediction the optimal representation, particularly for dynamic urban scenes? We propose EVolSplat4D, a feed-forward 3D Gaussian prediction framework for both static and dynamic urban scenes that goes beyond per-pixel representations. Our key idea is to directly learn scene representations in 3D Euclidean space for close-range regions and dynamic objects, while retaining pixel-aligned Gaussian prediction for far-range regions. This hybrid design enables multi-view consistent reconstruction for close-

range static volumes and dynamic objects while efficiently modeling unbounded regions.

Specifically, we decompose the scene into three components: the static close-range volume, dynamic vehicles, and the far-field scenery, and design a dedicated feed-forward module for each. For the static close-range volume, we depart from per-pixel-aligned prediction and instead first construct a global 3D semantic field by lifting 2D semantic features (DINO Oquab et al (2023)) across multiple frames into Euclidean space using noisy depth estimates. Geometry is then predicted directly in 3D by decoding this field into Gaussian parameters with a 3D convolutional network, yielding view-consistent structure. Given the predicted geometry, appearance is queried via an occlusion-aware image-based rendering (IBR) module that leverages semantic features to blend multi-view colors robustly. For dynamic vehicles, we adopt the same principle of avoiding per-pixel-aligned prediction but operate in an object-centric canonical space. Each moving instance is disentangled from the static scene and mapped to a canonical coordinate system, utilizing estimated 3D bounding boxes to parameterize time-dependent rigid motions. While these bounding boxes may be noisy, our motion-adjusted IBR module robustly aggregates appearance features across multiple timestamps and viewpoints, mitigating misalignment and enabling consistent, feed-forward dynamic reconstruction. Finally, far-range regions and the sky are handled by a per-pixel Gaussian decoder based on a cross-view attention 2D U-Net. To obtain the final im-

age, we integrate the predicted Gaussians from all three modules and perform α -blending, allowing efficient generalization to the full scene.

We summarize our contributions as follows:

- We introduce EvolSplat4D, a novel Gaussian-based framework for unbounded urban scenes that factorizes the environment into three generalizable components: close-range volume, dynamic vehicles, and far-field scenery. Our method supports both static and dynamic feed-forward reconstruction, enabling real-time, photo-realistic rendering from sparse input images.
- We propose a volume-based 3D Gaussian reconstruction approach for close-range static regions, in which geometry and appearance predictions are decoupled. Geometry is predicted in a view-consistent 3D space across multiple frames, while a semantic-enhanced IBR module robustly infers appearance and mitigates noise in the geometry.
- We leverage predicted 3D bounding boxes to model dynamic actors in object-centric canonical spaces and propose a motion-adjusted IBR module for generalizable 4D reconstruction. By robustly aggregating temporal features, this module mitigates the effect of noisy 3D bounding boxes to enable high-fidelity rendering and controllable scenario editing.
- Extensive experiments on four datasets, KITTI-360, KITTI, Waymo, and PandaSet, demonstrate that EvolSplat4D accurately reconstructs dynamic scenes and consistently outperforms both per-scene optimization and feed-forward baselines.

This journal paper is an extension of a conference paper published at CVPR 2025, EVolSplat [Miao et al \(2025\)](#). In comparison to EVolSplat, which is limited to static reconstruction, we 1) incorporate additional geometric cues (e.g., 3D bounding boxes) and propose a novel motion-adjusted IBR technique to achieve unified feed-forward reconstruction for both static and dynamic scenes; 2) design a specialized far-field branch equipped with cross-view attention to improve the background fidelity; 3) integrate self-supervised semantic priors to augment the occlusion module for more robust detection of occluded regions, and 4) extensively enrich the experimental section by including new datasets (KITTI and PandaSet) and conduct additional scene editing experiments.

2 Related Work

2.1 Novel View Synthesis for Urban Scenes

Static Scenes: The rapid development of radiance field techniques [Kerbl et al \(2023\)](#); [Mildenhall et al \(2021\)](#) have significantly advanced novel view synthesis for driving scenes. These approaches represent street scenes as implicit neural fields [Guo et al \(2023\)](#); [Xie et al \(2023\)](#); [Rematas et al \(2022\)](#); [Tancik et al \(2022\)](#); [Wang et al \(2023\)](#) or anisotropic 3D Gaussians [Lin et al \(2024\)](#); [Liu et al \(2024\)](#); [Kerbl et al \(2024\)](#), achieving expressive synthesis. A few works [Xie et al \(2023\)](#); [Rematas et al \(2022\)](#); [Yang et al \(2023b\)](#) leverage sparse vehicle-mounted LiDAR sensors to boost the training and learn a robust geometry. Other works also incorporate additional semantic and geometry cues as priors or supervision to enhance scene comprehension, including semantic understanding [Fu et al \(2023\)](#); [Kundu et al \(2022\)](#) and geometric constraints [Cui et al \(2025\)](#); [Guo et al \(2023\)](#). However, these approaches primarily target static scenes and struggle to handle dynamic agents in urban environments.

Dynamic Scenes: Subsequent methods have addressed dynamic elements by constructing scene graphs, where each moving instance is separated from the static background using annotated 3D bounding boxes, as adopted in [Zhou et al \(2024a,b\)](#); [Yan et al \(2024\)](#); [Chen et al \(2024c\)](#); [Khan et al \(2024\)](#); [Wu et al \(2023\)](#); [Ost et al \(2021\)](#). While this yields more accurate reconstruction and facilitates object-level editing, it requires expensive per-scene optimization. In contrast, our feed-forward method aims to perform efficient reconstruction on novel dynamic scenes. Other approaches eliminate the need for 3D bounding box by learning to decompose the static and dynamic components in a self-supervised manner. SUDS [Turki et al \(2023\)](#) and EmerNeRF [Yang et al \(2023a\)](#) model motion implicitly in 4D spacetime between frames, using foundation models like DINO [Oquab et al \(2023\)](#) to establish correspondences in challenging conditions. In parallel, Dynamic Gaussian methods learning attributes like displacement [Huang et al \(2024\)](#) or lifespan [Chen et al \(2023\)](#); [Peng et al \(2025\)](#) for each primitive, distinguishing static from dynamic ones through available 2D image observations. Despite these advances, separation remains incomplete [Fan et al \(2025\)](#). In our research, we utilize predicted 3D bounding box to decouple scenes into a static reference space and time-dependent deformations, facilitating pose editing and novel pose synthesis applications that are challenging with 4D spacetime representations.

2.2 2D Supervised Feed-Forward Reconstruction

To perform feed-forward reconstruction, researchers train neural networks across large-scale datasets to gain domain-specific prior knowledge. These methods [Yu et al \(2021\)](#); [Charatan et al \(2024\)](#); [Chen et al \(2024b\)](#); [Zhang et al \(2024a, 2025a\)](#); [Szymanowicz et al \(2024b\)](#) have evolved to work with sparse image sets and can directly reconstruct scenes via fast feed-forward inference. Generalizable NeRF performs ray-based rendering and estimates the 3D radiance field of scenes, which enables superior cross-dataset generalization capabilities in both small [Chen et al \(2021\)](#); [Wang et al \(2021\)](#); [Yu et al \(2021\)](#) and large baseline [Xu et al \(2023\)](#); [Du et al \(2023\)](#) settings. However, NeRF based methods are notoriously slow to render. Another line of work directly predicts pixel-aligned 3D Gaussians from sparse reference images [Szymanowicz et al \(2024a,b\)](#); [Zhang et al \(2025a\)](#); [Chen et al \(2024b\)](#); [Liang et al \(2024\)](#); [Chen et al \(2025a\)](#). These methods either utilize an epipolar transformer [Charatan et al \(2024\)](#); [Wewer et al \(2024\)](#) or construct local cost volumes [Chen et al \(2024b\)](#); [Zhang et al \(2024a\)](#); [Liu et al \(2025\)](#) for learning geometry. However, most of these methods focus on small-scale scenes and require overlaps in the input images, making them difficult to apply in driving scenes with large camera movements and small parallax. Our method predicts the global scene representation instead of per-pixel Gaussian by accumulating and refining depth information in 3D space. This improves global consistency and reduces ghosting artifacts when rendering new images. VolSplat [Wang et al \(2025d\)](#) and Omni-Scene [Wei et al \(2025\)](#) also adopt a volume-based architecture to predict the Gaussians but are designed for static scenes. In comparison, we leverage 3D bounding box tracks to enable feed-forward inference on 4D environments.

In related work, STORM [Yang et al \(2024a\)](#) and DrivingRecon [Lu et al \(2024\)](#) perform feed-forward 4D reconstruction in driving environments but still adhere to the per-pixel Gaussian paradigm. The geometric inconsistencies of these methods are more pronounced in close-range regions due to stronger viewpoint-induced parallax, while far-range regions are inherently less sensitive to such misalignment. Flux4D [Wang et al \(2025a\)](#) initializes Gaussians from LiDAR points and employs a 3D U-Net to recover the scene, but it requires additional iterative refinement to improve background appearance and reconstruction quality. Motivated by these observations, EVolSplat4D adopts a hybrid architecture that employs a volume-based representation to ensure close-range geometric consistency, while retaining pixel-aligned regression for synthesizing high-fidelity far-field scenery.

2.3 3D Supervised Feed-Forward Reconstruction

Recent approaches in 3D vision, such as DUST3R [Wang et al \(2024\)](#) and VGGT [Wang et al \(2025b\)](#), replace traditional multi-stage pipelines with a single large-scale model to directly regress geometric structures including camera poses and depth from images. Follow-up works [Zhang et al \(2024b\)](#); [Wang et al \(2025c\)](#); [Sucar et al \(2025\)](#); [Jiang et al \(2025b\)](#); [Feng et al \(2025\)](#); [Fei et al \(2024\)](#) extend this line of methods to tackle dynamic content. Despite the progress, these methods produce only point clouds, lacking the ability for high-quality view synthesis. To bridge this gap, some approaches [Sun et al \(2025b\)](#); [Zhang et al \(2025b\)](#); [Lin et al \(2025\)](#) further integrate an additional prediction head to infer pixel-aligned 3D Gaussians, but they are still restricted to static scenes. Moreover, all these methods heavily rely on significant amounts of training data with 3D annotations for supervision, and such data is hard to collect for dynamic scenes, especially in the real world. In contrast, EVolSplat4D achieves end-to-end reconstruction from sparse views while relying solely on readily available 2D images for supervision.

3 Method

Taking sparse images and tracked 3D bounding boxes predicted from LiDAR observations as inputs, we aim to learn a feed-forward model that directly outputs a set of 3D Gaussians for both static and dynamic regions. Our framework supports both static and dynamic street scene reconstruction, with optional fine-tuning for further improvement. An overview of EVolSplat4D is provided in Fig. 2. We decompose the scene into three components: a close-range volume, dynamic vehicles, and a far-field scenery, each represented by a set of 3D Gaussians, denoted as \mathcal{G}^{cr} , \mathcal{G}^{dyn} , and \mathcal{G}^{far} , respectively. The **close-range volume** refers to a predefined spatial region that covers the vehicle’s trajectory while excluding **dynamic actors**, whereas the **far-field scenery** corresponds to the far-range regions and sky outside this volume.

We develop three feed-forward branches, one for each component. For the close-range volume branch, we initialize global primitives from depth priors and semantic image features, which are then transformed into an encoding volume to predict geometry of 3D Gaussian primitives, followed by an occlusion-aware IBR module for appearance parameters (Section 3.2). For dynamic actors, we model each actor in a canonical space and propose a motion-adjusted IBR module to regress Gaussian attributes (Section 3.3). For the far-field scenery in street scenes, we train a generalizable U-Net with

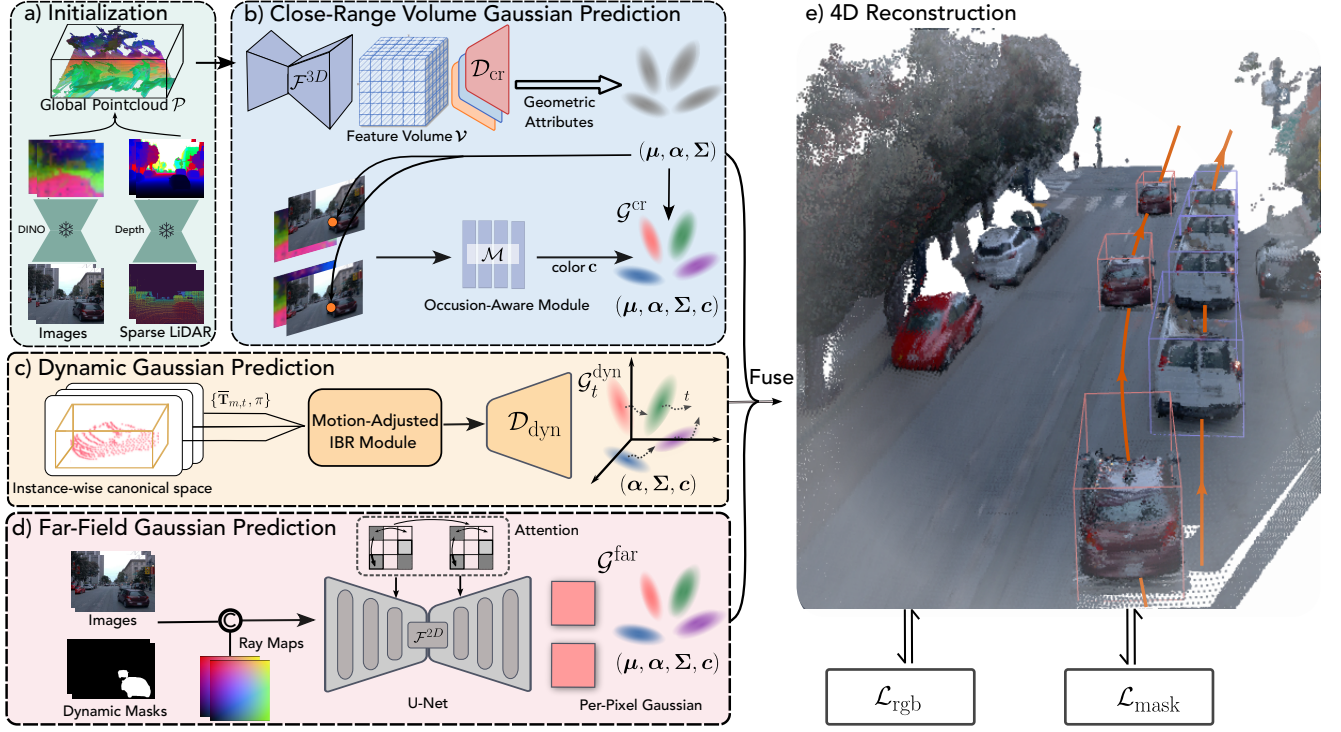


Fig. 2: Method Overview. We reconstruct urban scenes by disentangling them as close-range volume, dynamic actors, and far-field scenery, predicting 3D Gaussians of each in a feed-forward manner. a) Given a set of images, we initialize our model with the pretrained depth model and DINO feature extractor. b) In close-range volume, we leverage the 3D context of \mathcal{F}^{3D} to predict the geometry attributes of 3D Gaussians and project the 3D Gaussians to the reference views to retrieve 2D context, including color window and visibility maps to decode their color. c) For dynamic actors, we model each instance using an instance-wise canonical space and perform feed-forward reconstitution through our proposed motion-adjusted IBR module. d) To model far-range regions, we employ a 2D U-Net backbone \mathcal{F}^{2D} with cross-view self-attention to aggregate information from nearby reference images and predict per-pixel Gaussians. e) The composition of the three parts leads to our full model for unbounded scenes.

cross-view attention mechanisms to predict pixel-aligned Gaussians (Section 3.4). Finally, these three parts are fused to represent unbounded street scenes (Section 3.5).

3.1 Preliminary

3D Gaussian Splatting: 3D Gaussian Splatting Kerbl et al (2023) explicitly parameterizes the 3D radiance field of the underlying scene as a collection of 3D Gaussians primitives $\mathcal{G} = \{(\mu_i, \alpha_i, \Sigma_i, c_i)\}_{i=1}^G$, with attributes: a mean position μ_i , an opacity α_i , a covariance matrix Σ_i and view-dependent color c_i (computed by spherical harmonics). The 3D covariance matrix $\Sigma \in \mathbb{R}^{3 \times 3}$ of each Gaussian is defined as:

$$\Sigma = RSS^T R^T \quad (1)$$

where R denotes the rotation (also represented as quaternion \mathbf{q}) and S denotes the scale (comprising s_x, s_y, s_z).

A 3D Gaussian is defined as follows:

$$G(\mathbf{x}) = \alpha \exp \left(-\frac{1}{2} (\mathbf{x} - \mu)^T \Sigma^{-1} (\mathbf{x} - \mu) \right) \quad (2)$$

This efficient representation avoids expensive volumetric sampling and enables high-speed rendering. To render the image from a particular viewpoint, 3DGS employs the tile-based rasterizer for Gaussian splats to pre-sort and blend the ordered primitives using differentiable volumetric rendering:

$$C = \sum_{i \in G} c_i \alpha_i \prod_{j=1}^{i-1} (1 - \alpha_j) \quad (3)$$

3.2 Close-Range Volumetric Gaussian branch

Global Point Cloud Initialization: To overcome the limitations of per-pixel representations, our method leverages depth priors to construct a global point cloud, which serves as the foundation for decoding a set of

multi-view consistent 3D Gaussians via a 3D CNN. We first unproject multi-view depth maps into a shared world coordinate system using their respective camera poses. Specifically, the depth maps $\{D_n\}_{n=1}^N$ for N input images are generated from sparse LiDAR observations using an off-the-shelf depth completion model Wang et al (2025e). Notably, our framework is depth-modality agnostic: our ablation studies demonstrate that both metric monocular depth predictions and sparse LiDAR completion yield comparable performance.

Regarding the attributes of this global point cloud, we opt for semantic features over raw RGB information to facilitate the prediction of refined geometry in the subsequent volumetric branch. We extract feature maps $\{F_n\}_{n=1}^N$ from the N input images using DINOv2 Oquab et al (2023). To ensure memory efficiency, Principal Component Analysis (PCA) is applied to compress these features into 16 channels. These feature maps are then lifted into 3D space and accumulated to construct a global semantic point cloud $\mathcal{P} \in \mathbb{R}^{N_p \times 16}$ in world coordinates, utilizing calibrated intrinsic matrices $\{\mathbf{K}_n\}_{n=1}^N$ and extrinsic matrices $\{\mathbf{T}_n = \mathbf{R}_n \mid \mathbf{t}_n\}_{n=1}^N$. The construction process is defined as:

$$\mathcal{P} = \bigcup_{n=1}^N \pi^{-1}(F_n, D_n, \mathbf{T}_n, \mathbf{K}_n) \quad (4)$$

where π^{-1} denotes pixel unprojection.

Unlike previous pixel-aligned 3DGS methods that inevitably generate redundant primitives in overlapping regions, our approach avoids this issue by operating directly in Euclidean space. We apply a spatial uniform filter to the raw points \mathcal{P} to explicitly prune primitives in high-density regions, thereby eliminating redundancy while preserving the underlying scene structure. Additionally, we employ a statistical filter to remove floaters. Most importantly, we introduce a learned refinement module to optimize primitive locations, as detailed in the subsequent section.

Neural Volume Prediction: We draw inspiration from Huang et al (2023); Chen et al (2024a) and map \mathcal{P} into a 3D latent neural volume using a generalizable 3D CNN that captures prior knowledge across scenes. Specifically, we voxelize the global point cloud \mathcal{P} into a sparse tensor and apply an efficient sparse U-Net-style 3D CNN \mathcal{F}^{3D} to produce a neural feature volume $\mathcal{V} \in \mathbb{R}^{H \times W \times D \times C}$, where $H \times W \times D$ denotes the spatial resolution and C the feature dimension. The sparse 3D ConvNet adopts an encoder-decoder architecture with a low-resolution bottleneck, and skip connections are used to preserve both local and global information:

$$\mathcal{V} = \mathcal{F}^{3D}(\mathcal{P}). \quad (5)$$

Different from other feed-forward GS works using a 2D image-to-image neural network to encode the scene, this 3D latent representation helps integrate volumetric context in different network layers for faithful reconstructions. Note that the output feature volume \mathcal{V} is aligned with the world coordinate system.

Gaussian Geometry Decoding: We decode the geometry attributes of N_p 3D Gaussians based on the feature volume \mathcal{V} , taking the scene point cloud \mathcal{P} as the initial Gaussian centers, i.e., $\mu_i^{init} = \mathbf{p}_i \in \mathcal{P}$. For each μ_i^{init} , we query a latent feature from \mathcal{V} using trilinear interpolation, and map it to a position offset $\Delta\mu_i$, opacity α_i , and covariance matrix Σ_i based on three independent MLP heads, respectively.

Considering that the network is supposed to gradually move the 3D Gaussians to the correct locations over the training process, we aim to use the updated locations $\mu_i^{init} + \Delta\mu_i$ to query the feature volume to decode α_i and Σ_i . This encourages the network to predict α_i and Σ_i at a more accurate position, i.e., near the object surface. However, we don't have the direct 3D supervision of $\Delta\mu_i$. Therefore, we build an updating rule, with which $\Delta\mu_i$ converges at the end of the training by learning from 2D rendering losses.

Specifically, we keep track of the network's prediction of $\Delta\mu_i$ from the last iteration as $\Delta\mu_i^{prev}$. For each iteration, we query \mathcal{V} at $\mu_i^{init} + \Delta\mu_i^{prev}$, obtaining a feature vector \mathbf{h}_i :

$$\mathbf{h}_i = \mathcal{V}(\mu_i^{init} + \Delta\mu_i^{prev}) \quad (6)$$

$$\alpha_i = \mathcal{D}_{cr}^{opa}(\mathbf{h}_i), \quad \Sigma_i = \mathcal{D}_{cr}^{cov}(\mathbf{h}_i) \quad (7)$$

$$\Delta\mu_i = \text{Tanh}(\mathcal{D}_{cr}^{pos}(\mathbf{h}_i)) \cdot v_{size}, \quad \mu_i = \mu_{init} + \Delta\mu_i \quad (8)$$

where \mathcal{D}_{cr}^{opa} , \mathcal{D}_{cr}^{cov} and \mathcal{D}_{cr}^{pos} denote MLP heads, and μ_i, α_i and Σ_i are subsequently used for rendering. Here, the output of \mathcal{D}_{cr}^{pos} is passed through a $\text{Tanh}()$ activation function, and then scaled by the voxel size v_{size} to yield the final adjustment. Note that this leads to a recursive formulation of $\Delta\mu_i$ where its value depends on the output of the previous estimations. We show that $\Delta\mu_i$ is stabilized to a stationary point at infinite training iterations in the supplementary. During inference, we initialize $\Delta\mu_i^{prev} = 0$, recursively execute Eq. 6 and Eq. 8, and use the converged point to query α_i and Σ_i . We empirically find that it is sufficient to only execute the recursion twice to obtain a converged $\Delta\mu_i$.

As shown in our ablation experiment, the inclusion of offset allows our method to compensate for noisy positions and enhances the representational capacity.

Occlusion-Aware Appearance Modeling: While our volume-based representation effectively ensures geometric consistency, the inherent downsampling of primitives may result in the loss of high-frequency appear-

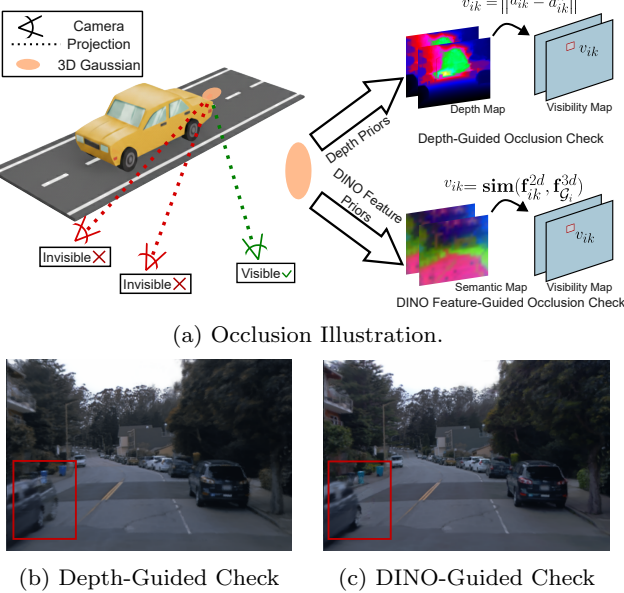


Fig. 3: **Occlusion Illustration.** a) One Gaussian in 3D space may retrieve inaccurate color information from 2D reference images due to occlusions. b) The previous method [Miao et al \(2025\)](#) uses depth priors to check occlusions, which may suffer from inaccurate monocular depth predictions. c) In contrast, EVolSplat4D comprises robust DINO priors to reduce the impact of invisible colors to enhance rendering quality.

ance details. To capture these fine-grained textures, we employ an image-based rendering (IBR) approach to learn Gaussian appearance. However, two primary challenges arise in this setting: 1) imprecise initialization of Gaussian centers leads to inaccurate 2D projections, and 2) even with accurate centers, retrieved colors can be inconsistent due to significant occlusions. To address these issues, we extend the projection location into a local sampling window and propose an occlusion-aware module to robustly blend multi-view colors.

For each Gaussian primitive, we project its center μ_i to the nearby K reference frames and sample local colors $\{\mathbf{c}_{ik} \in \mathbb{R}^{W \times W \times 3}\}_{k=1}^K$ using a $W \times W$ window centered at the 2D projection. This allows integrating additional 2D texture information and improves robustness against noisy 3D Gaussian locations. In practice, we find $W = 3$ to be effective (see ablation study).

To handle occlusions, we explore two visibility check options, illustrated in Fig. 3a: (1) depth-guided and (2) DINO feature-guided. The depth-guided check, utilized in our conference version, leverages the retrieved monocular depth D_n as a pseudo-ground-truth reference to identify occluded regions. Specifically, let d_{ik} denote the projected depth of Gaussian center μ_i from the k -th camera viewpoint. We estimate visibility based

on the residual between the projected depth and the retrieved depth d_{ik}^n from D_n via $v_{ik} = \|d_{ik} - d_{ik}^n\|$. However, this method remains sensitive to inaccuracies in monocular depth estimation within complex environments (see Fig. 3b). In contrast, our DINO feature-guided check relies on the intuition that a 3D Gaussian and its unoccluded 2D projection should maintain semantic similarity, thereby removing the dependency on potentially noisy depth priors. We compute the cosine similarity $\text{sim}(\cdot, \cdot)$ between the unprojected 3D feature \mathbf{f}_i^{3d} stored in \mathcal{P} and the retrieved 2D features \mathbf{f}_{ik}^{2d} from the k -th reference frame. The final visibility v_{ik} is then obtained via a temperature-scaled Softmax normalized over all K reference frames:

$$v_{ik} = \frac{\exp(\text{sim}(\mathbf{f}_{ik}^{2d}, \mathbf{f}_i^{3d})/\tau)}{\sum_{k'=1}^K \exp(\text{sim}(\mathbf{f}_{ik'}^{2d}, \mathbf{f}_i^{3d})/\tau)}, \quad (9)$$

where $\tau = 0.1$ in our experiments. This approach effectively identifies inconsistent observations due to occlusion and focuses on visible views (see Fig. 3c).

Instead of discarding invisible projections with a manual threshold, we concatenate the local window colors and their visibility and feed them into a three-layer MLP \mathcal{M} , which outputs the color represented using spherical harmonics (SH) coefficients:

$$\mathbf{c}_i = \mathcal{M}(\{\mathbf{c}_{ik}, v_{ik}\}_{k=1}^K). \quad (10)$$

3.3 Generalizable Dynamic Gaussian branch

Dynamic Gaussian Modeling: To enable flexible control and model the movements of dynamic instances (e.g. cars, trucks) without sacrificing reconstruction quality, we model each instance using an instance-wise canonical space and time-varying rigid transformation. This formulation ensures that each moving instance is represented independently in a static canonical space across all frames, facilitating information accumulation. For a scene containing M moving actors, we utilize an off-the-shelf detector [Wu et al \(2021\)](#) and tracker [Wu et al \(2022\)](#) to generate 3D bounding boxes and temporal poses $\overline{\mathbf{T}}_{m,t} \in \text{SE}(3)$ for each actor $m \in \{1, \dots, M\}$. While the tracking is performed on LiDAR observations following the common practice of dynamic urban reconstruction methods [Yan et al \(2024\)](#); [Chen et al \(2025b\)](#); [Tonderski et al \(2024\)](#), the 3D points within these bounding boxes can be derived from either LiDAR observations or monocular depth predictions. By leveraging these tracked poses, we transform the 3D points within the bounding boxes from all frames into a unified local object coordinate system and aggregate them to form a semantic point cloud with DINO features

$\bar{\mathcal{P}}_m^{\text{dyn}} \in \mathbb{R}^{N_d \times 16}$ in the canonical space. This canonical representation captures the time-invariant geometry of each rigid actor. At a target time t , the points are transformed back into world space by applying the corresponding pose transformation:

$$\mathcal{P}_{m,t}^{\text{dyn}} = \bar{\mathbf{T}}_{m,t} \bar{\mathcal{P}}_m^{\text{dyn}} \quad (11)$$

Motion-Adjusted Image-Based Rendering: Unlike our static branch, which employs a 3D CNN to refine geometry through learned position offsets, we utilize the accumulated canonical point locations directly as the Gaussian centers μ for dynamic actors. We find that while thin structures or complex topologies in the static close-range volume benefit more from learned geometric refinement, dynamic vehicles possess more regularized geometries where multi-frame aggregation in a constrained canonical space provides a sufficiently stable foundation. Consequently, we task our motion-adjusted IBR module to predict all other Gaussian attributes, including opacity α , covariance Σ , and color \mathbf{c} . To effectively compensate for any remaining inaccuracies in μ or the tracked bounding boxes, we also leverage a window-based IBR design.

Specifically, our motion-adjusted IBR accounts for rigid object motion, as illustrated in Fig. 4. Taking a triplet $\{t-1, t, t+1\}$ and their corresponding rigid transformations $\bar{\mathbf{T}}_{m,t-1}$, $\bar{\mathbf{T}}_{m,t}$, and $\bar{\mathbf{T}}_{m,t+1}$ as an example, we apply Eq. 11 to place the canonical points into the world space corresponding to the precise timestamp of each captured frame. Subsequently, the projection operator π maps these time-adjusted 3D points onto the respective 2D reference image planes to query color cues. This motion-adjusted projection ensures that each dynamic point gathers coherent appearance information across multiple timestamps.

Similar to Section 3.2, we retrieve appearance cues $\{\mathbf{c}_{ik}\}_{k=1}^K$ and visibility terms $\{v_{ik}\}_{k=1}^K$ from DINO features within a predefined window to enhance robustness against noisy predicted 3D bounding boxes. Our ablation study demonstrates that this window-based sampling strategy achieves performance comparable to using ground-truth bounding boxes. The aggregated 2D features are then processed by a shared three-layer MLP for all M moving actors, which serves as a dynamic Gaussian decoder \mathcal{D}_{dyn} to predict the final Gaussian attributes $\mathcal{G}_t^{\text{dyn}} = \{(\alpha_i, \Sigma_i, \mathbf{c}_i)\}_{i=1}^{N_d}$.

3.4 Generalizable Far-Field Branch

As our volume-based representation covers only limited close-range street scenes, it is insufficient for the unbounded region, such as the sky and distant landscapes

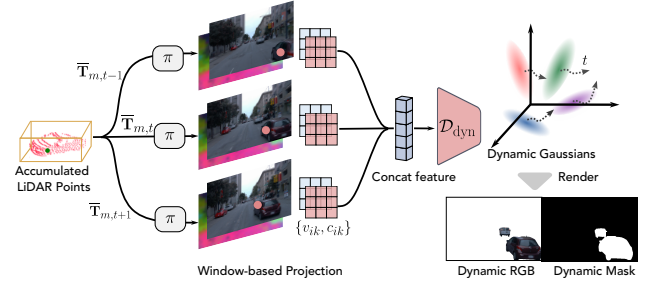


Fig. 4: Motion Adjusted IBR. LiDAR points in the canonical space for an instance m are transformed using time-specific poses and projected into reference frames. A Window-based Projection strategy then samples coherent appearance features c_{ik} and visibility map v_{ik} , which are input to the dynamic Gaussian decoder \mathcal{D}_{dyn} . The decoder regresses the 3D Gaussian attributes for each point, enabling the final rendering of the dynamic object’s image and binary mask.

(often over 100 meters away). Previous works [Chen et al \(2023\)](#); [Ye et al \(2024a\)](#); [Xu et al \(2024\)](#); [Rematas et al \(2022\)](#); [Yan et al \(2024\)](#) construct an environment map conditioned on input direction for a special scene, yet struggle to handle multiple scenes simultaneously. To this end, we introduce our generalizable far-field branch tailored for driving scenes to model infinite sky and background landscapes.

Inspired by LGM [Tang et al \(2024\)](#), we employ a 2D U-Net backbone $\mathcal{F}^{2\text{D}}$ with cross-view self-attention to aggregate information from nearby reference images and predict per-pixel Gaussians. The input to the $\mathcal{F}^{2\text{D}}$ is a 10-channel feature map, where each feature vector \mathbf{e}_i is formed by concatenating its RGB color \mathbf{c}_i , a binary mask \mathbf{b}_i , and its Plücker ray embeddings:

$$\mathbf{e}_i = \{\mathbf{c}_i, \mathbf{b}_i, \mathbf{o}_i \times \mathbf{r}_i, \mathbf{r}_i\} \quad (12)$$

Here, \mathbf{o}_i and \mathbf{r}_i denote the ray origin and direction, respectively. The binary mask \mathbf{b}_i , provided by our dynamic Gaussian branch (Section 3.3), is utilized to suppress interference from dynamic actors, preventing them from being erroneously baked into the static background representation.

Within the U-Net architecture, self-attention is restricted to the two deepest layers to maintain computational efficiency while capturing long-range dependencies. Each pixel of the output feature map is interpreted as a 3D Gaussian primitive with 12 channels representing RGB color $\mathbf{c}_i \in \mathbb{R}^3$, scale $\mathbf{s}_i \in \mathbb{R}^3$, a rotation quaternion $\mathbf{q}_i \in \mathbb{R}^4$, opacity $\alpha_i \in \mathbb{R}$, and a 1-channel ray distance $z_i \in \mathbb{R}$. The Gaussian center is defined as $\mu_i = \mathbf{o}_i + z_i \mathbf{r}_i$. The final far-field representation \mathcal{G}^{far} is obtained by merging the Gaussians predicted from all

K views. Although this model effectively captures far-range regions, our ablation study demonstrates that it is insufficient for modeling close-range structures with the same fidelity as our volume-based representation.

3.5 Compositional Rendering

The integration of these three specialized components, the close-range volume, dynamic actors, and the far-field scenery, constitutes our comprehensive model for unbounded street scenes. To synthesize the scene from a target viewpoint at time t , we unify these primitives into a single representation: $\mathcal{G}_t^{\text{scene}} = \mathcal{G}_t^{\text{cr}} \cup \mathcal{G}_t^{\text{dyn}} \cup \mathcal{G}_t^{\text{far}}$. These composite Gaussians are rendered onto the 2D image plane using standard 3D Gaussian Splatting rasterization. Specifically, α -blending is first employed to accumulate color and opacity for the combined close-range volume and dynamic actors:

$$\mathbf{C}^{(\text{cr+dyn})} = \sum_{i \in \mathcal{G}_t^{\text{cr}}, \mathcal{G}_t^{\text{dyn}}} c_i \alpha_i \prod_{j=1}^{i-1} (1 - \alpha_j) \quad (13)$$

$$\mathbf{O}^{(\text{cr+dyn})} = \sum_{i \in \mathcal{G}_t^{\text{cr}}, \mathcal{G}_t^{\text{dyn}}} \alpha_i \prod_{j=1}^{i-1} (1 - \alpha_j) \quad (14)$$

Finally, we integrate the far-field rendering \mathbf{C}_{far} as a background layer to reconstruct the full scene:

$$\mathbf{C} = \mathbf{C}^{(\text{cr+dyn})} + (1 - \mathbf{O}^{(\text{cr+dyn})}) \mathbf{C}_{\text{far}} \quad (15)$$

4 Implementation Details

4.1 Loss Function

Our model is trained in an end-to-end manner, jointly optimizing the scene representation across various driving scenarios. The total loss function is defined as:

$$\mathcal{L} = \mathcal{L}_{\text{rgb}} + \lambda_m \mathcal{L}_{\text{mask}} \quad (16)$$

where λ_m is a balancing weight. In the following, we elaborate on the individual loss components.

Photometric loss: We apply L1 and SSIM losses between a rendered image \mathbf{C} and the GT image $\hat{\mathbf{C}}$ for supervision of RGB rendering. The balance term λ_{SSIM} is set to 0.2 in our setting.

$$\mathcal{L}_{\text{rgb}} = (1 - \lambda_{\text{SSIM}}) \|\mathbf{C} - \hat{\mathbf{C}}\|_1 + \lambda_{\text{SSIM}} \text{SSIM}(\mathbf{C}, \hat{\mathbf{C}}) \quad (17)$$

Decomposition loss: A primary challenge in our hybrid representation is ensuring that the close-range

volume (\mathcal{G}^{cr}) and the far-field background (\mathcal{G}^{far}) exclusively model their respective portions of the scene. To prevent geometric ambiguity, we introduce a mask loss $\mathcal{L}_{\text{mask}}$ to enforce explicit spatial separation between these components:

$$\mathcal{L}_{\text{mask}} = \|\mathbf{O}^{(\text{cr})} - \hat{\mathbf{O}}\|_1 \quad (18)$$

The binary mask $\hat{\mathbf{O}}$ is generated by projecting the initial global point cloud \mathcal{P} onto the image plane, where pixels corresponding to the close-range volume are assigned a value of 1 and otherwise set to 0. This supervision encourages the close-range branch to maintain high opacity in its designated region while penalizing the far-field branch for erroneously rendering content within the foreground volume.

4.2 Fine-Tuning

Once fine-tuning is applied, our method can achieve photorealism on par with or surpassing other per-scene optimization methods, leveraging powerful pretrained weights. Specifically, we first predict a set of 3D Gaussian primitives for initialization via a direct feed-forward process, where both the geometry and color attributes are generated. The fine-tuning process follows the vanilla 3DGS, where we optimize all Gaussian attributes and refine tracked bounding boxes directly. We also enable the growing and pruning of 3D primitives during fine-tuning. During fine-tuning, the number of Gaussians is significantly reduced, as the initial feed-forward Gaussians are redundant. As a result, our model maintains high fidelity while reducing memory consumption. We demonstrate that the pretrained priors accelerate network training and enable faster convergence compared to other test-time optimization methods.

4.3 Training Details

We train EVolSplat4D end-to-end on multiple scenes using the Adam optimizer [Kingma and Ba \(2014\)](#) with learning rate 1×10^{-3} . We use torchsparse [Tang et al \(2022\)](#) as the implementation of 3D sparse convolution and choose gsplat [Ye et al \(2024b\)](#) as our Gaussian rasterization library. We set the SH degree to 1 for simplicity, following StreetGaussian [Yan et al \(2024\)](#). During training, we set $\lambda_m = 0.1$ as loss weights in our work. For each iteration, our model randomly selects a single image from a random scene as supervision.

Method	KITTI-360 (In-Domain)			Waymo (Out-of-Domain)			FPS↑	Mem.(GB)↓ (Render res.: 376×1408)
	PSNR↑	SSIM↑	LPIPS↓	PSNR↑	SSIM↑	LPIPS↓		
MVSNeRF Chen et al (2021)	18.44	0.638	0.317	17.86	0.595	0.433	0.025	12.03
MuRF Xu et al (2023)	22.77	0.780	0.229	23.33	0.770	0.269	0.31	26.45
EDUS Miao et al (2024)	22.13	0.745	0.178	23.18	0.745	0.164	0.14	5.75
PixelSplat Charatan et al (2024)	19.41	0.584	0.357	16.65	0.541	0.579	81.58	26.75
MVSplat Chen et al (2024b)	21.22	0.695	0.268	21.33	0.665	0.308	70.46	16.14
DepthSplat Xu et al (2025)	21.44	0.687	0.265	20.95	0.664	0.400	76.24	17.62
AnySplat Jiang et al (2025a)	20.09	0.629	0.264	24.58	0.784	0.193	79.36	22.05
EVolSplat	23.26	0.797	0.179	23.43	0.786	0.202	83.81	10.41
EVolSplat4D	23.36	0.798	0.177	24.43	0.829	0.184	82.46	10.98

Table 1: **Quantitative results on Static Scenes** with other feed-forward baselines on both KITTI-360 and Waymo open datasets. All models are trained on the KITTI-360 dataset using a drop50% sparsity level. Metrics are averaged on five validation scenes without any finetuning. It is also worth noting that our method is more memory efficient compared with other 3DGS-based methods.

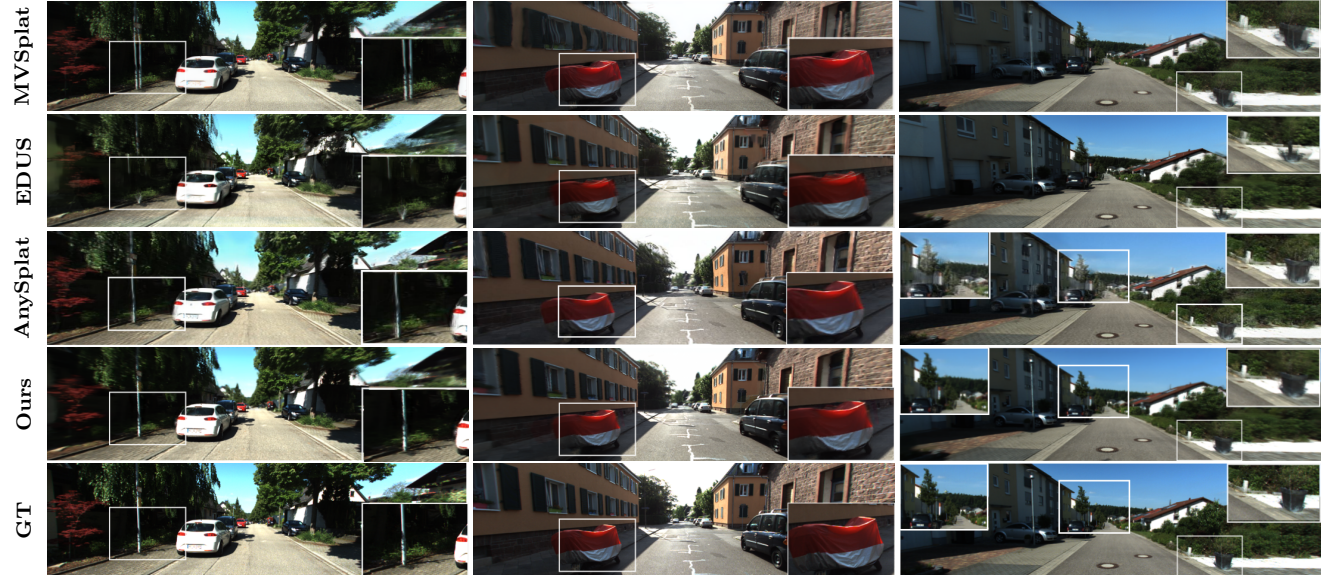


Fig. 5: **Qualitative Comparison** with feed-forward baselines on the KITTI-360 dataset.

5 Experiment

5.1 Dataset

Static Scenes: We pretrain our static model on the KITTI-360 dataset [Liao et al \(2022\)](#). Specifically, we begin with 160 sequences from the KITTI-360 (same as in our conference version [Miao et al \(2025\)](#)) to learn robust representations for static scenes reconstruction. To simulate sparse driving scenarios, we apply a **50% drop rate** (Drop 50%) during all static training and validation. Additionally, we evaluate the zero-shot generalization performance on Waymo [Sun et al \(2020\)](#).

Dynamic Scenes: Since KITTI-360 scenarios are primarily static, we supplement them with 181 motion-rich sequences from the Waymo [Sun et al \(2020\)](#) and KITTI [Geiger et al \(2013\)](#) to improve generalization to dynamics. This results in a total of 341 training sequences, each containing 60 images. For validation, we use a total of 10 clips as an in-domain dataset, consisting of 5 sequences from the KITTI validation set and 5 from Waymo NOTR [Yang et al \(2023a\)](#), ensuring no overlap with the training data. Furthermore, we utilize PandaSet [Xiao et al \(2021\)](#) as an out-of-domain dataset to evaluate the zero-shot generalization performance in dynamic environments. We follow the experimental setup from STORM [Yang et al \(2024a\)](#) and use a more

sparse **80% drop rate** (Drop 80%) for all sequences, which enables us to assess the robustness of our model to varying sparsity levels. As we find that our dynamic baseline methods suffer from high memory cost when training with high-resolution images, we downsample input images for all methods: 4 \times for Waymo and PandaSet and 2 \times for KITTI and KITTI-360.

5.2 Experimental Setup

Metrics: We evaluate novel view synthesis on both interpolated and extrapolated views. For interpolated evaluation, we adopt existing evaluation protocols, including PSNR, SSIM, and LPIPS, for quantitative assessments. For the extrapolated views, quantitative metrics like PSNR that require ground-truth images cannot be computed. Instead, we use the Kernel Inception Distance (KID) Bińkowski et al (2018) to measure the similarity in distribution between extrapolated views and real captured images. Regarding the computation efficiency, we report the inference memory usage (GB) and frame per second (FPS) on the same device (NVIDIA RTX 5880) to ensure a fair comparison.

Volume Setup: For the Close-Range Volume, we set its Z-axis to cover the vehicle’s forward trajectory with a length of 80m, whereas the height (Y-axis) and width (X-axis) is 12.8m and 40m, respectively. The input point cloud is voxelized with a voxel size of (0.1m, 0.1m, 0.1m), resulting in the volume dimension of 128 \times 400 \times 800. Notably, our 3D CNN effectively handles arbitrary volume size well during inference.

Baselines: We compare EVolSplat4D with several representative feed-forward methods across both static and dynamic scenes. For static scenes, we evaluate against NeRF-based approaches including MVSNeRF Chen et al (2021), MuRF Xu et al (2023), EDUS Miao et al (2024), and 3DGS-based approaches, including MVSplat Chen et al (2024b), PixelSplat Charatan et al (2024), Depth-Splat Xu et al (2025) and AnySplat Jiang et al (2025a). In dynamic scenes, we compare with recent feed-forward 4DGS methods like STORM Yang et al (2024a) and DrivingRecon Lu et al (2024). Unless stated otherwise, we train and evaluate all feed-forward models using the same data as EVolSplat4D. The only exception is AnySplat Jiang et al (2025a), which builds upon VGGT Wang et al (2025b) and is pre-trained on large indoor and outdoor datasets. Therefore, we directly use its official checkpoint without retraining. Notably, since AnySplat cannot accept pose inputs, we follow its protocol to estimate poses for the test views before evaluation. Additionally, we compare the NVS quality and reconstruc-

tion time with other per-scene optimization methods designed for urban scenes, including SUDS Turki et al (2023), StreetGaussian Yan et al (2024), OmniRe Chen et al (2024c), EmerNeRF Yang et al (2023a) and DeSiRe-GS Peng et al (2025).

5.3 Evaluation on Static Scenes

In-Domain Rendering Quality: Table 1 and Fig. 5 present quantitative and qualitative comparison results for feed-forward inference in static scenes of KITTI-360, evaluated under a 50% drop rate. Our proposed EVolSplat4D achieves superior photorealism on this in-domain setting compared to state-of-the-art feed-forward NeRF- and 3DGS-based approaches. While EDUS and MuRF show promising metrics, EDUS suffers from artifacts in thin structures, and MuRF struggles with geometry in texture-less areas, such as roads, due to its reliance on feature mapping. MVSplat and Depth-Splat utilize Transformers for per-frame depth estimation, which can result in inconsistent 3D Gaussian primitives and ghost artifacts under large camera movements. For AnySplat, which operates in a zero-shot setting here as it was pre-trained on separate large-scale datasets, the sparse views on KITTI-360 lead to inaccurate geometric reconstruction and artifacts in far-field background regions.

Compared with our conference version, EVolSplat, we replace the hemisphere background model with our Generalizable Far-Field Branch, which improves background fidelity and final results. It is worth noting that while our unified model utilizes LiDAR priors to initialize the close-range volume branch, our depth ablation in Table 8 demonstrates that replacing these with monocular metric depth (e.g., Metric3D) yields comparable performance. This confirms that the superiority of EVolSplat4D stems from our architectural design rather than the sensor modality.

Zero-Shot Inference on Waymo: To further verify the generalization capability of the evaluated models, we conduct experiments on an unseen dataset, the Waymo Open dataset Sun et al (2020). This evaluation represents an out-of-domain setting for all methods. Specifically, all models except for AnySplat are trained exclusively on KITTI-360. AnySplat is uniquely advantaged in this comparison as it is pre-trained on a broader collection of large-scale indoor and outdoor scenes. During evaluation, we set the image resolution to 640 \times 960 and assess the resulting rendering quality. As demonstrated in Table 1, our method achieves superior performance across most benchmarks. While AnySplat reports a slightly higher PSNR on Waymo than

Method	KITTI (In-Domain)			Waymo (In-Domain)			PandaSet (Out-of-Domain)			FPS↑	Mem.(GB)↓
	PSNR↑	SSIM↑	LPIPS↓	PSNR↑	SSIM↑	LPIPS↓	PSNR↑	SSIM↑	LPIPS↓	(Render res.: 320×480)	
DrivingRecon Lu et al (2024)	19.50	0.597	0.283	20.21	0.572	0.277	14.92	0.506	0.389	190.78	9.48
STORM Yang et al (2024a)	18.96	0.658	0.256	23.76	0.764	0.182	23.13	0.766	0.207	178.57	22.31
AnySplat Jiang et al (2025a)	16.31	0.596	0.268	21.84	0.694	0.231	22.34	0.725	0.273	161.11	11.42
EVolSplat	16.52	0.583	0.275	22.86	0.753	0.201	23.32	0.746	0.253	212.42	6.41
EVolSplat4D	20.76	0.738	0.162	26.32	0.822	0.121	26.27	0.823	0.132	201.06	6.71

Table 2: **Quantitative results on Dynamic Scenes** with feed-forward baselines. Metrics are averaged on five validation scenes without any finetuning in drop80% sparsity level. Our EVolSplat4D generalizes better than all the baseline in a large margin on both **in-domain** (KITTI, Waymo) and **out-of-domain** (PandaSet) datasets.



Fig. 6: **Qualitative Comparisons** with baselines for feed-forward inference on the KITTI dataset. The rendering images are downsampled 2x to 188×621.

on KITTI-360, this is largely due to Waymo’s higher capture frequency: the dataset maintains larger view overlap than KITTI-360, facilitating easier reconstruction. Nevertheless, EVolSplat4D outperforms AnySplat in terms of SSIM and LPIPS despite using much less training data, demonstrating strong generalization capability and superior perceptual quality. Finally, we observe that EDUS yields the lowest LPIPS on Waymo. This can be attributed to its NeRF-based architecture, which often excels at modeling fine-grained details compared to splatting-based approaches. More qualitative results are provided in the supplementary material.

Model Efficiency: We report the memory consumption during inference on a full-resolution 376×1408 image of KITTI-360 in Table 1. MuRF and PixelSplat fail to infer with full-resolution on a consumer GPU (24GB) since their transformer architecture requires heavy computational resources. In contrast, our method leverages

an efficient sparse 3DCNN for feed-forward reconstruction with only 10.98GB usage, demonstrating superior memory efficiency and practical utility. Additionally, we note that EDUS consumes 5.75GB of memory for inference as its NeRF-based representation only casts 4096 rays each iteration, resulting in lower memory usage but significantly slow rendering speed (0.14fps).

5.4 Evaluation on Dynamic Scenes

In-Domain Rendering Quality: Table 2, Fig. 6, and Fig. 7 present quantitative and qualitative comparison results for in-domain feed-forward inference on dynamic scenes. To ensure a fair comparison, all baselines except for AnySplat [Jiang et al \(2025a\)](#) are trained on a unified dataset comprised of sequences from KITTI [Geiger et al \(2013\)](#), KITTI-360 [Liao et al \(2022\)](#), and Waymo [Sun et al \(2020\)](#). Note that our model achieves



Fig. 7: **Qualitative Comparisons** with baselines for feed-forward inference on the Waymo Open dataset and PandaSet. Each column represents a different method, while each pair of rows corresponds to a different dataset. The rendering images resolution are 480×320 for Waymo and 480×270 for PandaSet.

the best performance among all the baselines. Specifically, DrivingRecon [Lu et al \(2024\)](#) employs temporal cross-attention to generate per-pixel Gaussians but struggles to reliably regress Gaussian attributes and motion across timestamps, leading to suboptimal rendering quality. STORM [Yang et al \(2024a\)](#) leverages self-supervised learning to decompose scene dynamics and predict scene flow, yet still produces noticeable artifacts in dynamic regions. Although AnySplat [Jiang et al \(2025a\)](#) and EVolSplat perform well on static scenes, they lack dedicated mechanisms for modeling dynamic content, resulting in significant motion blur.

Zero-Shot Inference on PandaSet: We further evaluate the zero-shot generalization of all feed-forward baselines on PandaSet, with results reported in Table 2. On this out-of-domain dataset, our method consistently outperforms prior baselines across all visual metrics by a large margin, demonstrating strong robustness and generalization. The qualitative results in Fig. 7 further support this conclusion: DrivingRecon still produces blurry results, and STORM sometimes fails to capture distant buildings in PandaSet.

We further evaluate view extrapolation quality by reporting the KID score under a 1 m lane-shift setting, where no ground-truth images are available (see Table 3). Our method achieves superior performance in this challenging extrapolation scenario. As shown in

Method	KITTI	Waymo	PandaSet
DriveRecon Lu et al (2024)	0.350	0.315	0.383
STORM Yang et al (2024a)	0.104	0.080	0.102
EVolSplat4D (Ours)	0.062	0.063	0.080

Table 3: **Quantitative Comparison of View Extrapolation Quality.** We report averaged KID \downarrow (lower values indicate better performance) on diverse datasets without finetuning in Drop 80% sparsity level.

Method	PSNR \uparrow	SSIM \uparrow	LPIPS \downarrow	Rec. Time \downarrow
SUDS Turki et al (2023)	25.03	0.813	0.167	45min
EmerNeRF Yang et al (2023a)	27.03	0.886	0.069	21min
StreetGaussian Yan et al (2024)	27.27	0.891	0.057	7min
DeSiRe-GS Peng et al (2025)	27.35	0.889	0.094	14min
OmniRe Chen et al (2024c)	28.16	0.912	0.051	9min
EVolSplat4D (Ours _{0-iter})	25.39	0.841	0.119	1.3s
EVolSplat4D (Ours _{1000-iter})	28.29	0.903	0.048	3min 40s

Table 4: **Comparison with Optimization-Based** baselines on 3 sequences of the Waymo NOTR dataset under the Drop 80% sparsity level. The **Rec. Time** refers to the reconstruction time needed to reach convergence and achieve the reported metrics.

Fig. 8, EVolSplat4D produces high-fidelity images with clear lane markings, avoiding the distortion and blur observed in STORM.



Fig. 8: **Extrapolated Views Qualitative Comparison** with STORM on PandaSet.

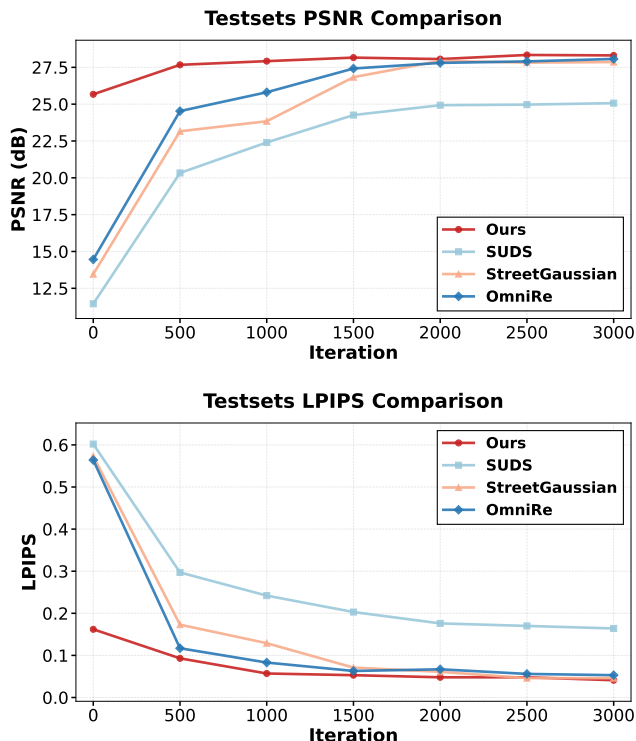


Fig. 9: **Convergence Analysis** on the Waymo Dataset. We plot PSNR and LPIPS on one test set at different training steps. Compared with optimization-based baselines, our method with generalizable priors converges faster (≈ 1000 steps) and achieves better PSNR.

5.5 Comparison with Optimization-Based Methods

We further compare our model’s fine-tuning performance on dynamic scenes against other test-time optimization methods under the challenge sparse 80% drop rate, reporting the PSNR and LPIPS curves in Fig. 9.

As shown in Table 4, the baselines exhibit clear limitations under this sparse setting. NeRF-based meth-

	PSNR \uparrow	SSIM \uparrow	LPIPS \downarrow
w/o volume branch	27.02	0.839	0.132
w/o pixel branch	26.29	0.817	0.194
w/o motion-adjusted IBR	26.77	0.837	0.121
w/o Occ. check	27.33	0.844	0.113
w/o $\mathcal{L}_{\text{mask}}$	27.45	0.847	0.108
Full	27.78	0.856	0.102

Table 5: **Ablation Analysis** of method components.

ods, including SUDS [Turki et al \(2023\)](#) and EmerNeRF [Yang et al \(2023a\)](#), struggle to decompose dynamic elements in a fully self-supervised manner, resulting in significant artifacts with sparse inputs (see supplementary video). While 3DGS-based baselines such as StreetGaussian [Yan et al \(2024\)](#) and OmniRe [Chen et al \(2024c\)](#) achieve better results by leveraging 3D bounding box priors, they still require reconstructing the entire scene from scratch, leading to long training time. Note that EmerNeRF, StreetGaussian, and OmniRe all require LiDAR observations as input, ensuring a fair comparison. DeSiRe-GS [Peng et al \(2025\)](#) adopts a complex two-stage pipeline that distills 2D motion into Gaussian space based on the PVG [Chen et al \(2023\)](#) representation, resulting in excessive training time (14 minutes). In contrast, our model enables rapid initialization in just 1.3s (denoted as $\text{Ours}_{0\text{-iter}}$ in Table 4) and supports subsequent fine-tuning to further enhance reconstruction quality, converging within ≈ 1000 steps to achieve superior fidelity.

5.6 Ablation Study and Analysis

For fast ablation experiments, we train on a smaller subset of sequences from the Waymo dataset. The resulting pretrained models are then evaluated in a feed-forward manner under an 80% drop rate sparsity setting to ablate the design choices of EVolSplat4D. Table 5 and Fig. 10 present the quantitative and qualitative results, respectively.

Effectiveness of Hybrid Representation: We employ a hybrid representation that integrates 3D Gaussians from both volumetric and pixel-aligned branches to model static environments. To validate this architectural choice, we evaluate two variants, one omitting the volumetric branch and another omitting the far-field branch. In the first variant that excludes the 3D volumetric CNN, the pixel branch is responsible for modeling the entire static scene, including both the far-field background and the close-range volume, yielding a configuration conceptually similar to MVSplat. This setup

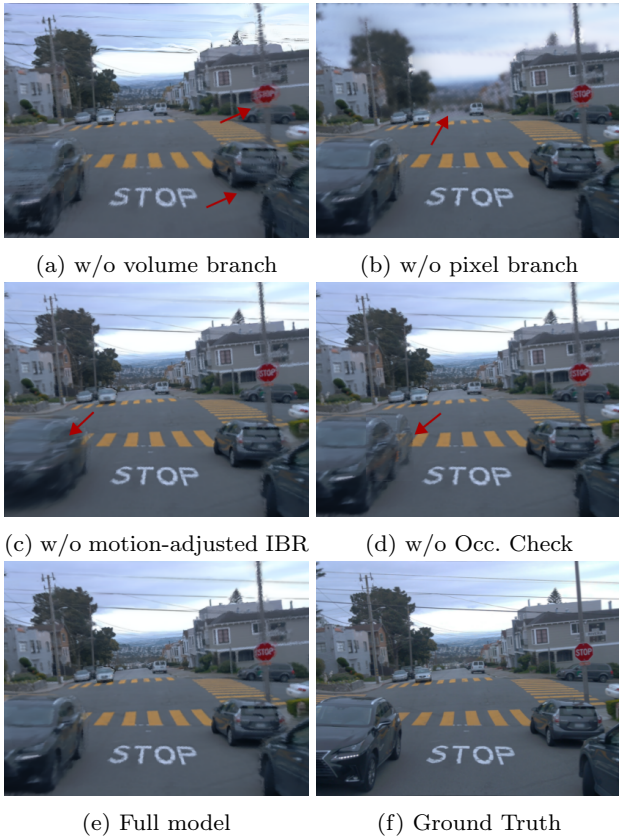


Fig. 10: **Qualitative Results of Ablation Study.** We represent rendering images via feed-forward inference on one novel scene.

leads to a performance degradation of 0.76 dB in PSNR, 0.017 in SSIM, and 0.03 in LPIPS. Under this per-pixel scheme, novel views of the close-range region exhibit ghosting artifacts (see Fig. 10a) caused by redundant and inconsistent Gaussian predictions in overlapping image areas.

Conversely, we evaluate a variant without the pixel branch, replacing it with the simple hemisphere background model from our conference version, EVolSplat Miao et al (2025). This model only roughly approximates the geometry of the far-field scenery, failing to capture complex structures and sometimes resulting in artifacts in the background region (see Figure 10b).

Effectiveness of Motion-Adjusted IBR: We now validate the importance of our motion-adjusted IBR strategy, a core component of the Generalizable Dynamic Gaussian branch (Section 3.3). Our full method transforms an actor’s canonical points into the world space corresponding to each reference frame’s specific timestamp before querying appearance features. We compare this to a baseline variant that omits this temporal alignment, which directly projects primitives at the tar-

Setting	PSNR \uparrow	SSIM \uparrow	LPIPS \downarrow
$W = 1$, Pred bbx	27.45	0.850	0.115
$W = 3$, Pred bbx	27.78	0.856	0.102
$W = 5$, Pred bbx	27.56	0.853	0.106
$W = 3$, Gt bbx	27.73	0.860	0.095

Table 6: **Ablation study on window size (W) and bounding box source.** Using $W = 3$ with predicted bounding boxes (Pred bbx) yields the best results among window sizes. Notably, this performance is comparable to using ground-truth bounding boxes (Gt bbx).



Fig. 11: **Qualitative Results of Scene Decompose Loss.** The images are rendered only from the Gaussians within the close-range region. Without $\mathcal{L}_{\text{mask}}$, the far-field pixel branch partially models the close-range building, causing Gaussians from the \mathcal{G}^{cr} to be semi-transparent.

get time to nearby reference images. The results in Table 5 show a clear decrease in rendering quality (PSNR 27.78 \rightarrow 26.77). As seen in Fig. 10c, this performance drop is mostly due to the severely degraded reconstruction quality of the dynamic vehicles. This demonstrates that our motion-adjusted IBR strategy is essential for querying consistent appearance features across time, facilitating high-fidelity dynamic rendering.

Effectiveness of Occlusion Check: To investigate the occlusion check importance, we perform a study that removes the visibility maps v_{ik} and instead naively aggregates all 2D colors retrieved from K reference views to learn Gaussian appearance. As illustrated in Fig. 10d, the rendering quality in occluded regions suffers from noticeable blurriness. By incorporating DINO feature as priors, our model effectively removes the impact of the occlusion-caused feature, resulting in an overall improvement of about 0.45dB PSNR as reported in Table 5.

Effectiveness of Scene Decomposition: We now evaluate the effectiveness of our Scene Decomposition loss $\mathcal{L}_{\text{mask}}$, which is designed to enforce spatial separation between the close-range (\mathcal{G}^{cr}) and far-field (\mathcal{G}^{far})

branches. As reported in Table 5 (w/o $\mathcal{L}_{\text{mask}}$), while removing this loss has only a minor impact (0.33dB drop in PSNR) on the rendering fidelity, clean decomposition is crucial for maintaining geometric accuracy of the close-range volume. Without it, the network may still synthesize plausible images but fail to disentangle the scene geometry. As shown in the rendering of the close-range volume in Fig. 11, a part of Gaussians \mathcal{G}^{cr} in the close-range volume branch becomes semi-transparent without $\mathcal{L}_{\text{mask}}$.

Analysis of Color Window: We further investigate the impact of the projection window size W on reconstruction quality. As shown in Table 6, we compare three window configurations ($W = \{1, 3, 5\}$) through feed-forward inference on novel scenes. At $W = 1$, each Gaussian retrieves appearance information from only a single pixel per reference frame, resulting in the lowest PSNR. This performance drop stems from inaccurate Gaussian positions or noisy bounding box priors, which lead to misaligned 2D projections. Increasing the window size to $W = 3$ improves image quality by integrating local texture information, which effectively compensates for these projection inaccuracies. However, at $W = 5$, the inclusion of redundant color information introduces blurring, leading to an increase in LPIPS and higher memory overhead.

Importantly, this window-based sampling strategy also mitigates the effects of noisy 3D bounding box predictions for dynamic actors. A comparison between Row 2 and Row 4 in Table 6 validates this robustness. Our full model, utilizing predicted boxes (27.78 dB PSNR), achieves performance on par with the variant using ground-truth bounding boxes (27.73 dB PSNR), with only a negligible 0.004 difference in SSIM. This experiment confirms that our aggregation strategy successfully compensates for the noise inherent in automated object tracking, enabling robust and high-fidelity 4D reconstruction.

Analysis of $\Delta\mu_i$ Update: As mentioned in the Section 3.2, $\Delta\mu_i$ depends on the previous estimation $\Delta\mu_i^{\text{prev}}$, but it stabilizes at a stationary point after infinite training iterations. Note that $\mathcal{D}_{\text{cr}}^{\text{pos}}$ is designed to continually decode the offset Δ wrt. μ_{init} , even at the ideal location, avoiding an infinite loop caused by toggling between the ideal offset and zero. We further conduct experiments by recursively updating the offsets ($i = 0, 1, 2, 3$) during inference to verify their convergence. As reported in Table 7, our pretrained model successfully refines the noisy primitive’s position after the first inference (increasing PSNR by approximately 0.52 dB) and maintains a stable value of 27.78dB even with additional updates.

	PSNR↑	SSIM↑	LPIPS↓
$i = 0$	27.260	0.833	0.142
$i = 1$	27.787	0.856	0.102
$i = 2$	27.781	0.856	0.102
$i = 3$	27.785	0.856	0.102

Table 7: **Ablation Study** on recursion of $\Delta\mu_i$. The results are tested on the Waymo dataset.

Modality	Method	PSNR↑	SSIM↑	LPIPS↓
Monocular Pred.	UniDepth Piccinelli et al (2024)	27.59	0.854	0.105
LiDAR Compl.	Metric3D Yin et al (2023)	27.86	0.859	0.104
	Prior Depth Anything Wang et al (2025e)	27.78	0.856	0.102

Table 8: **Depth Sensitivity Experiment.** The results are averaged on five testsets from the Waymo dataset.

As discussed in Section 3.2, the position offset $\Delta\mu_i$ depends on the preceding estimation $\Delta\mu_i^{\text{prev}}$, yet it converges to a stationary point over infinite training iterations. Importantly, the MLP head $\mathcal{D}_{\text{cr}}^{\text{pos}}$ is designed to consistently decode the offset Δ relative to the initial position μ_{init} . This design choice ensures that even when the primitive reaches its ideal location, the system avoids infinite oscillations or "toggling" between the ideal offset and zero. To verify this convergence empirically, we conduct experiments by recursively updating the offsets ($i = \{0, 1, 2, 3\}$) during the inference phase. As reported in Table 7, our pretrained model successfully refines the noisy primitive locations after a single refinement step—increasing PSNR by approximately 0.52 dB—and maintains a stable performance of 27.78 dB across subsequent updates.

Analysis of Depth Modularity: We further validate the robustness of our framework with respect to the choice of depth initialization. Specifically, we replace our default LiDAR priors with monocular predictions from pre-trained models (UniDepth [Piccinelli et al \(2024\)](#) and Metric3D [Yin et al \(2023\)](#)). In these monocular variants, we utilize the estimated depth maps to initialize both the global point cloud and dynamic vehicles in canonical space. As shown in Table 8, the results are highly consistent across all input modularities. Our model achieves nearly identical performance regardless of the depth source, with all PSNR approximately 27dB and SSIM at 0.86. These results confirm that our system is flexible and can be initialized with depth maps from various distributions.

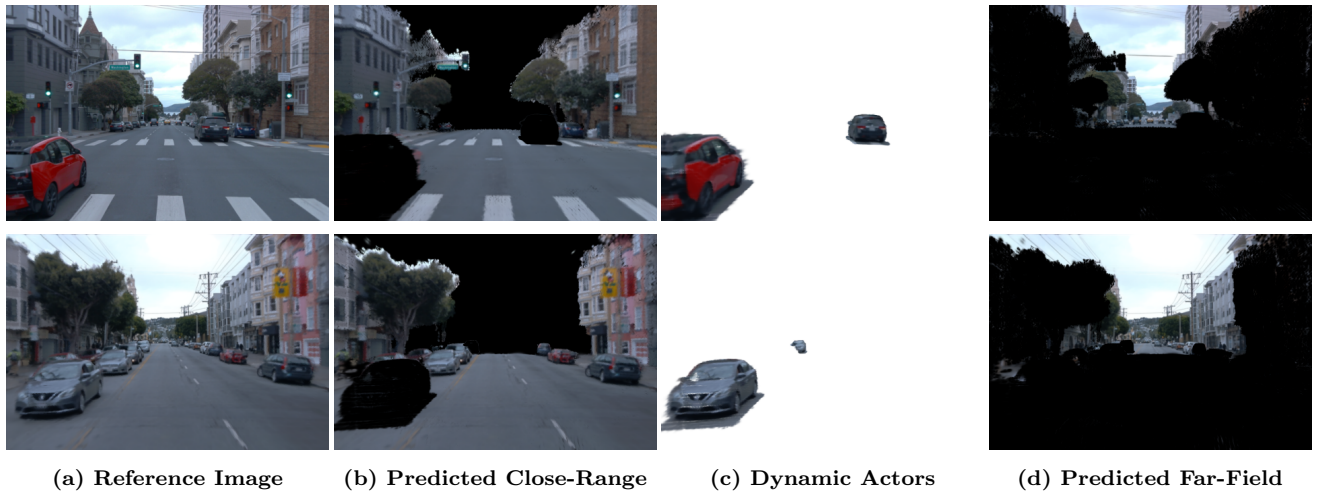


Fig. 12: **Scene Decomposition on Waymo.** Our approach enables clear decomposition of the close-range volume, dynamic actors, and the far-field scenery.

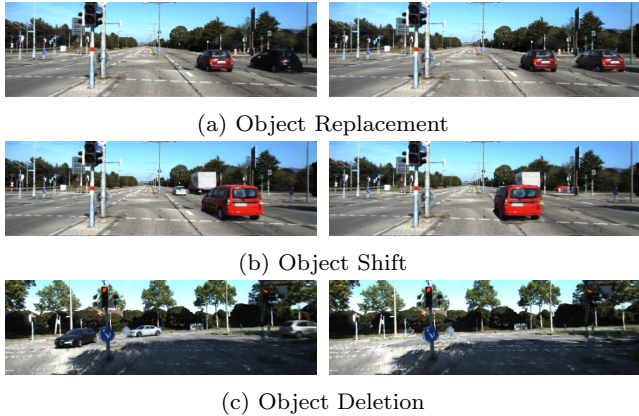


Fig. 13: **Scene Editing on KITTI.** Images in the first and second columns represent the results before and after editing.

5.7 Application

Scene Editing: Our instance-aware scene representation facilitates a variety of scenario-level editing operations. Leveraging the disentangled 3D Gaussians, we can seamlessly replace a specific vehicle with another instance (Fig. 13a), translate actors to novel positions (Fig. 13b), or entirely remove all dynamic objects from the environment (Fig. 13c). These capabilities demonstrate the flexibility of our object-centric canonical modeling for simulation purposes.

Scene Decomposition: The proposed hybrid reconstruction framework captures comprehensive 4D geometry by factorizing the environment into three constituent components: the **close-range volume**, **dynamic actors**, and the **far-field scenery**. As illustrated in Fig. 12, our method successfully disentangles these ele-

ments into independent representations, yielding cleanly decomposed layers suitable for downstream autonomous driving tasks.

6 Limitations

Our method has several limitations. First, while our core method is not inherently dependent on active sensors, we currently utilize LiDAR-derived 3D bounding boxes to define the object-centric canonical spaces. This design follows common practice in per-scene optimization Yan et al (2024); Tonderski et al (2024) and is motivated by the higher accuracy of LiDAR-based detection, which significantly outperforms existing RGB-only methods Sun et al (2025a); Hu et al (2022) by about 40% mAP on the KITTI 3D detection benchmark Geiger et al (2013). However, our method remains architecturally decoupled from the LiDAR sensor: it processes RGB images and depth priors for feature learning and rendering, where monocular-based depth priors yield rendering quality comparable to LiDAR-based alternatives. This modularity ensures that the approach remains functional using only camera data, provided that 3D bounding boxes are supplied by an external module. As monocular 3D detection performance continues to bridge the gap with LiDAR-based methods, our approach can be seamlessly transitioned to a fully camera-only pipeline. Future work will explore the end-to-end integration of vision-based detection and tracking.

Secondly, despite that our method produces stable extrapolated rendering results, we observe a performance decline in large-baseline extrapolation experiments (e.g., translation > 3m). While the close-range

volume maintains robust synthesis quality, the performance in the far-field tends to degrade. This stems from the difference in geometric quality: the close-range branch leverages explicit metric depth for initialization, thus achieving high geometric fidelity and better generalization to extrapolated views. In contrast, the far-field branch is supervised solely by rendering loss without explicit depth priors. While reasonable rendering quality can be observed during interpolation, the synthesis quality drops under large camera translations. A potential solution is to incorporate stronger depth priors [Yu et al \(2026\)](#) or external supervision to recover more plausible geometry for the background model.

Finally, we assume that all moving objects follow simple rigid motion, which may cause blurring for non-rigid moving actors (e.g., pedestrians). This could be addressed by incorporating non-rigid dynamic reconstruction methods [Yang et al \(2024b\)](#); [Mao et al \(2025\)](#) into our pipeline.

7 Conclusion

We propose EVolSplat4D, an efficient feed-forward approach for reconstructing challenging dynamic urban scenes. By effectively incorporating valuable geometry cues from LiDAR, we decompose the scene into three independent components: a static close-range volume, dynamic actors, and a far-field region, each handled by a dedicated generalizable module. Our compositional reconstruction model unifies both dynamic and static feed-forward reconstruction from sparse camera inputs. The practical applications of our method include rapid, multiple urban scene reconstruction, object manipulation, and high-fidelity scene decomposition. We believe that our method pushes the frontier of feed-forward models for unbounded autonomous driving scenes with complex geometry and motion.

Data Availability

All datasets analyzed during this study are publicly available in the following public repositories:

- **KITTI-360:** <https://www.cvlibs.net/datasets/kitti-360/>
- **KITTI:** <https://www.cvlibs.net/datasets/kitti/>
- **Waymo Open Dataset:** <https://waymo.com/open/>
- **PandaSet:** <https://pandaset.org/>

References

Bińkowski M, Sutherland DJ, Arbel M, Gretton A (2018) Demystifying mmd gans. arXiv preprint arXiv:180101401 11

Charatan D, Li SL, Tagliasacchi A, Sitzmann V (2024) pixelsplat: 3d gaussian splats from image pairs for scalable generalizable 3d reconstruction. In: Proceedings of the IEEE/CVF Conference on Computer Vision and Pattern Recognition, pp 19457–19467 2, 4, 10, 11

Chen A, Xu Z, Zhao F, Zhang X, Xiang F, Yu J, Su H (2021) Mvsnerf: Fast generalizable radiance field reconstruction from multi-view stereo. In: Proceedings of the IEEE/CVF International Conference on Computer Vision, pp 14124–14133 1, 4, 10, 11, 2

Chen A, Xu H, Esposito S, Tang S, Geiger A (2024a) Lara: Efficient large-baseline radiance fields. arXiv preprint arXiv:240704699 6

Chen Y, Gu C, Jiang J, Zhu X, Zhang L (2023) Periodic vibration gaussian: Dynamic urban scene reconstruction and real-time rendering. arXiv preprint arXiv:231118561 3, 8, 14

Chen Y, Xu H, Zheng C, Zhuang B, Pollefeys M, Geiger A, Cham TJ, Cai J (2024b) Mvsplat: Efficient 3d gaussian splatting from sparse multi-view images. arXiv preprint arXiv:240314627 2, 4, 10, 11

Chen Y, Wang J, Yang Z, Manivasagam S, Urtasun R (2025a) G3r: Gradient guided generalizable reconstruction. In: European Conference on Computer Vision, Springer, pp 305–323 4

Chen Y, Zhang J, Xie Z, Li W, Zhang F, Lu J, Zhang L (2025b) S-nerf++: Autonomous driving simulation via neural reconstruction and generation. IEEE Transactions on Pattern Analysis and Machine Intelligence 7

Chen Z, Yang J, Huang J, de Lutio R, Esturo JM, Ivanovic B, Litany O, Gojcic Z, Fidler S, Pavone M, et al (2024c) Omnidre: Omni urban scene reconstruction. arXiv preprint arXiv:240816760 3, 11, 13, 14, 4

Cui X, Ye W, Wang Y, Zhang G, Zhou W, He T, Li H (2025) Streetsurfgs: Scalable urban street surface reconstruction with planar-based gaussian splatting. IEEE Transactions on Circuits and Systems for Video Technology 3

Du Y, Smith C, Tewari A, Sitzmann V (2023) Learning to render novel views from wide-baseline stereo pairs. In: Proceedings of the IEEE/CVF Conference on Computer Vision and Pattern Recognition, pp 4970–4980 4

Fan J, Zeng X, Zhang J, Gong M, Yang Y, Tao D (2025) Advances in radiance field for dynamic scene: From neural field to gaussian field. arXiv preprint arXiv:250510049 3

Fei X, Zheng W, Duan Y, Zhan W, Tomizuka M, Keutzer K, Lu J (2024) Driv3r: Learning dense 4d reconstruction for autonomous driving. arXiv preprint

arXiv:241206777 4

Feng H, Zhang J, Wang Q, Ye Y, Yu P, Black MJ, Darrell T, Kanazawa A (2025) St4rtrack: Simultaneous 4d reconstruction and tracking in the world. arXiv preprint arXiv:250413152 4

Fu X, Zhang S, Chen T, Lu Y, Zhou X, Geiger A, Liao Y (2023) Panopticnerf-360: Panoramic 3d-to-2d label transfer in urban scenes. arXiv preprint arXiv:230910815 3

Geiger A, Lenz P, Stiller C, Urtasun R (2013) Vision meets robotics: The kitti dataset. *The international journal of robotics research* 32(11):1231–1237 10, 12, 17, 2

Guo J, Deng N, Li X, Bai Y, Shi B, Wang C, Ding C, Wang D, Li Y (2023) Streetsurf: Extending multi-view implicit surface reconstruction to street views. arXiv preprint arXiv:230604988 3

Hu HN, Yang YH, Fischer T, Darrell T, Yu F, Sun M (2022) Monocular quasi-dense 3d object tracking. *IEEE Transactions on Pattern Analysis and Machine Intelligence* 45(2):1992–2008 17

Huang D, Peng S, He T, Yang H, Zhou X, Ouyang W (2023) Ponder: Point cloud pre-training via neural rendering. In: Proceedings of the IEEE/CVF International Conference on Computer Vision, pp 16089–16098 6

Huang N, Wei X, Zheng W, An P, Lu M, Zhan W, Tomizuka M, Keutzer K, Zhang S (2024) S^3 gaussian: Self-supervised street gaussians for autonomous driving. arXiv preprint arXiv:240520323 3

Jiang L, Mao Y, Xu L, Lu T, Ren K, Jin Y, Xu X, Yu M, Pang J, Zhao F, Lin D, Dai B (2025a) Anysplat: Feed-forward 3d gaussian splatting from unconstrained views. *ACM Transactions on Graphics (TOG)* 44:1–16, URL <https://api.semanticscholar.org/CorpusID:278997106> 10, 11, 12, 13, 2

Jiang Z, Zheng C, Laina I, Larlus D, Vedaldi A (2025b) Geo4d: Leveraging video generators for geometric 4d scene reconstruction. arXiv preprint arXiv:250407961 4

Kerbl B, Kopanas G, Leimkühler T, Drettakis G (2023) 3d gaussian splatting for real-time radiance field rendering. *ACM Transactions on Graphics* 42(4) 1, 3, 5

Kerbl B, Meuleman A, Kopanas G, Wimmer M, Lanvin A, Drettakis G (2024) A hierarchical 3d gaussian representation for real-time rendering of very large datasets. *ACM Transactions on Graphics (TOG)* 43(4):1–15 1, 3

Khan M, Fazlali H, Sharma D, Cao T, Bai D, Ren Y, Liu B (2024) Autosplat: Constrained gaussian splatting for autonomous driving scene reconstruction. arXiv preprint arXiv:240702598 3

Kingma DP, Ba J (2014) Adam: A method for stochastic optimization. arXiv preprint arXiv:14126980 9

Kundu A, Genova K, Yin X, Fathi A, Pantofaru C, Guibas LJ, Tagliasacchi A, Dellaert F, Funkhouser T (2022) Panoptic neural fields: A semantic object-aware neural scene representation. In: Proceedings of the IEEE/CVF Conference on Computer Vision and Pattern Recognition, pp 12871–12881 3

Liang H, Ren J, Mirzaei A, Torralba A, Liu Z, Gilitschenski I, Fidler S, Oztireli C, Ling H, Gojcic Z, et al (2024) Feed-forward bullet-time reconstruction of dynamic scenes from monocular videos. arXiv preprint arXiv:241203526 4

Liao Y, Xie J, Geiger A (2022) Kitti-360: A novel dataset and benchmarks for urban scene understanding in 2d and 3d. *IEEE Transactions on Pattern Analysis and Machine Intelligence* 45(3):3292–3310 10, 12, 2

Lin H, Chen S, Liew JH, Chen DY, Li Z, Shi G, Feng J, Kang B (2025) Depth anything 3: Recovering the visual space from any views. URL <https://api.semanticscholar.org/CorpusID:282992334> 4

Lin J, Li Z, Tang X, Liu J, Liu S, Liu J, Lu Y, Wu X, Xu S, Yan Y, et al (2024) Vastgaussian: Vast 3d gaussians for large scene reconstruction. In: Proceedings of the IEEE/CVF Conference on Computer Vision and Pattern Recognition, pp 5166–5175 3

Liu T, Wang G, Hu S, Shen L, Ye X, Zang Y, Cao Z, Li W, Liu Z (2025) Mvsgaussian: Fast generalizable gaussian splatting reconstruction from multi-view stereo. In: European Conference on Computer Vision, Springer, pp 37–53 4

Liu Y, Guan H, Luo C, Fan L, Peng J, Zhang Z (2024) Citygaussian: Real-time high-quality large-scale scene rendering with gaussians. arXiv preprint arXiv:240401133 3

Lu H, Xu T, Zheng W, Zhang Y, Zhan W, Du D, Tomizuka M, Keutzer K, Chen Y (2024) Drivingrecon: Large 4d gaussian reconstruction model for autonomous driving. arXiv preprint arXiv:241209043 2, 4, 11, 12, 13, 3

Mao Y, Xiong R, Wang Y, Liao Y (2025) Unire: Unsupervised instance decomposition for dynamic urban scene reconstruction. arXiv preprint arXiv:250400763 18

Miao S, Huang J, Bai D, Qiu W, Liu B, Geiger A, Liao Y (2024) Efficient depth-guided urban view synthesis. In: European Conference on Computer Vision, Springer, pp 90–107 1, 10, 11, 2

Miao S, Huang J, Bai D, Yan X, Zhou H, Wang Y, Liu B, Geiger A, Liao Y (2025) Evolsplat: Efficient volume-based gaussian splatting for urban view synthesis. In: Proceedings of the Computer Vision and

Pattern Recognition Conference, pp 11286–11296 3, 7, 10, 15, 2, 4

Mildenhall B, Srinivasan PP, Tancik M, Barron JT, Ramamoorthi R, Ng R (2021) Nerf: Representing scenes as neural radiance fields for view synthesis. Communications of the ACM 65(1):99–106 1, 3

Quab M, Darct T, Moutakanni T, Vo H, Szafraniec M, Khalidov V, Fernandez P, Haziza D, Massa F, El-Nouby A, et al (2023) Dinov2: Learning robust visual features without supervision. arXiv preprint arXiv:230407193 2, 3, 6

Ost J, Mannan F, Thuerey N, Knodt J, Heide F (2021) Neural scene graphs for dynamic scenes. In: Proceedings of the IEEE/CVF Conference on Computer Vision and Pattern Recognition, pp 2856–2865 3

Peng C, Zhang C, Wang Y, Xu C, Xie Y, Zheng W, Keutzer K, Tomizuka M, Zhan W (2025) Desire-gs: 4d street gaussians for static-dynamic decomposition and surface reconstruction for urban driving scenes. In: Proceedings of the Computer Vision and Pattern Recognition Conference, pp 6782–6791 3, 11, 13, 14

Piccinelli L, Yang YH, Sakaridis C, Segu M, Li S, Van Gool L, Yu F (2024) Unidepth: Universal monocular metric depth estimation. In: Proceedings of the IEEE/CVF Conference on Computer Vision and Pattern Recognition, pp 10106–10116 16

Rematas K, Liu A, Srinivasan PP, Barron JT, Tagliasacchi A, Funkhouser T, Ferrari V (2022) Urban radiance fields. In: Proceedings of the IEEE/CVF Conference on Computer Vision and Pattern Recognition, pp 12932–12942 1, 3, 8

Sucar E, Lai Z, Insafutdinov E, Vedaldi A (2025) Dynamic point maps: A versatile representation for dynamic 3d reconstruction. arXiv preprint arXiv:250316318 4

Sun P, Kretzschmar H, Dotiwalla X, Chouard A, Patnaik V, Tsui P, Guo J, Zhou Y, Chai Y, Caine B, et al (2020) Scalability in perception for autonomous driving: Waymo open dataset. In: Proceedings of the IEEE/CVF conference on computer vision and pattern recognition, pp 2446–2454 10, 11, 12, 2

Sun W, Lin X, Shi Y, Zhang C, Wu H, Zheng S (2025a) Sparsedrive: End-to-end autonomous driving via sparse scene representation. In: 2025 IEEE International Conference on Robotics and Automation (ICRA), IEEE, pp 8795–8801 17

Sun X, Jiang H, Liu L, Nam S, Kang G, Wang X, Sui W, Su Z, Liu W, Wang X, Park E (2025b) Uni3r: Unified 3d reconstruction and semantic understanding via generalizable gaussian splatting from unposed multi-view images. ArXiv abs/2508.03643, URL <https://api.semanticscholar.org/CorpusID:280527217> 4

Szymanowicz S, Insafutdinov E, Zheng C, Campbell D, Henriques JF, Rupprecht C, Vedaldi A (2024a) Flash3d: Feed-forward generalisable 3d scene reconstruction from a single image. arXiv preprint arXiv:240604343 4

Szymanowicz S, Rupprecht C, Vedaldi A (2024b) Splatter image: Ultra-fast single-view 3d reconstruction. In: Proceedings of the IEEE/CVF Conference on Computer Vision and Pattern Recognition, pp 10208–10217 2, 4

Tancik M, Casser V, Yan X, Pradhan S, Mildenhall B, Srinivasan PP, Barron JT, Kretzschmar H (2022) Block-nerf: Scalable large scene neural view synthesis. In: Proceedings of the IEEE/CVF Conference on Computer Vision and Pattern Recognition, pp 8248–8258 3

Tang H, Liu Z, Li X, Lin Y, Han S (2022) TorchSparse: Efficient Point Cloud Inference Engine. In: Conference on Machine Learning and Systems (MLSys) 9

Tang J, Chen Z, Chen X, Wang T, Zeng G, Liu Z (2024) Lgm: Large multi-view gaussian model for high-resolution 3d content creation. In: European Conference on Computer Vision, Springer, pp 1–18 8

Tonderski A, Lindström C, Hess G, Ljungbergh W, Svensson L, Petersson C (2024) Neurad: Neural rendering for autonomous driving. In: Proceedings of the IEEE/CVF Conference on Computer Vision and Pattern Recognition, pp 14895–14904 7, 17

Turki H, Zhang JY, Ferroni F, Ramanan D (2023) Suds: Scalable urban dynamic scenes. In: Proceedings of the IEEE/CVF Conference on Computer Vision and Pattern Recognition, pp 12375–12385 3, 11, 13, 14, 4

Wang J, Che H, Chen Y, Yang Z, Goli L, Manivasagam S, Urtasun R (2025a) Flux4d: Flow-based unsupervised 4d reconstruction. arXiv preprint arXiv:251203210 4

Wang J, Chen M, Karaev N, Vedaldi A, Rupprecht C, Novotny D (2025b) Vggt: Visual geometry grounded transformer. In: Proceedings of the Computer Vision and Pattern Recognition Conference, pp 5294–5306 4, 11, 3

Wang P, Liu Y, Chen Z, Liu L, Liu Z, Komura T, Theobalt C, Wang W (2023) F2-nerf: Fast neural radiance field training with free camera trajectories. In: Proceedings of the IEEE/CVF Conference on Computer Vision and Pattern Recognition, pp 4150–4159 1, 3

Wang Q, Wang Z, Genova K, Srinivasan PP, Zhou H, Barron JT, Martin-Brualla R, Snavely N, Funkhouser T (2021) Ibrnet: Learning multi-view image-based rendering. In: Proceedings of the IEEE/CVF Conference on Computer Vision and Pattern Recognition,

pp 4690–4699 4

Wang Q, Zhang Y, Holynski A, Efros AA, Kanazawa A (2025c) Continuous 3d perception model with persistent state. In: Proceedings of the Computer Vision and Pattern Recognition Conference, pp 10510–10522 4

Wang S, Leroy V, Cabon Y, Chidlovskii B, Revaud J (2024) Dust3r: Geometric 3d vision made easy. In: Proceedings of the IEEE/CVF Conference on Computer Vision and Pattern Recognition, pp 20697–20709 4

Wang W, Chen Y, Zhang Z, Liu H, Wang H, Feng Z, Qin W, Zhu Z, Chen DY, Zhuang B (2025d) Volsplat: Rethinking feed-forward 3d gaussian splatting with voxel-aligned prediction. arXiv preprint arXiv:250919297 4

Wang Z, Chen S, Yang L, Wang J, Zhang Z, Zhao H, Zhao Z (2025e) Depth anything with any prior. arXiv preprint arXiv:250510565 6, 16

Wei D, Li Z, Liu P (2025) Omni-scene: Omni-gaussian representation for ego-centric sparse-view scene reconstruction. In: Proceedings of the Computer Vision and Pattern Recognition Conference, pp 22317–22327 4, 3

Wewer C, Raj K, Ilg E, Schiele B, Lenssen JE (2024) latentsplat: Autoencoding variational gaussians for fast generalizable 3d reconstruction. arXiv preprint arXiv:240316292 4

Wu H, Han W, Wen C, Li X, Wang C (2021) 3d multi-object tracking in point clouds based on prediction confidence-guided data association. *IEEE Transactions on Intelligent Transportation Systems* 23(6):5668–5677 7

Wu H, Deng J, Wen C, Li X, Wang C, Li J (2022) Casa: A cascade attention network for 3-d object detection from lidar point clouds. *IEEE Transactions on Geoscience and Remote Sensing* 60:1–11 7

Wu Z, Liu T, Luo L, Zhong Z, Chen J, Xiao H, Hou C, Lou H, Chen Y, Yang R, et al (2023) Mars: An instance-aware, modular and realistic simulator for autonomous driving. In: CAAI International Conference on Artificial Intelligence, Springer, pp 3–15 3, 2

Xiao P, Shao Z, Hao S, Zhang Z, Chai X, Jiao J, Li Z, Wu J, Sun K, Jiang K, et al (2021) Pandaset: Advanced sensor suite dataset for autonomous driving. In: 2021 IEEE international intelligent transportation systems conference (ITSC), IEEE, pp 3095–3101 10, 2

Xie Z, Zhang J, Li W, Zhang F, Zhang L (2023) S-nerf: Neural radiance fields for street views. arXiv preprint arXiv:230300749 3

Xu C, Kerr J, Kanazawa A (2024) Splatfacto-w: A nerfstudio implementation of gaussian splatting for unconstrained photo collections. arXiv preprint arXiv:240712306 8

Xu H, Chen A, Chen Y, Sakaridis C, Zhang Y, Pollefeys M, Geiger A, Yu F (2023) Murf: Multi-baseline radiance fields. arXiv preprint arXiv:231204565 1, 4, 10, 11, 2

Xu H, Peng S, Wang F, Blum H, Barath D, Geiger A, Pollefeys M (2025) Depthsplat: Connecting gaussian splatting and depth. In: Proceedings of the Computer Vision and Pattern Recognition Conference, pp 16453–16463 2, 10, 11

Yan Y, Lin H, Zhou C, Wang W, Sun H, Zhan K, Lang X, Zhou X, Peng S (2024) Street gaussians for modeling dynamic urban scenes. arXiv preprint arXiv:240101339 3, 7, 8, 9, 11, 13, 14, 17, 4

Yang J, Ivanovic B, Litany O, Weng X, Kim SW, Li B, Che T, Xu D, Fidler S, Pavone M, et al (2023a) Emernerf: Emergent spatial-temporal scene decomposition via self-supervision. arXiv preprint arXiv:231102077 3, 10, 11, 13, 14, 4

Yang J, Huang J, Chen Y, Wang Y, Li B, You Y, Sharma A, Igl M, Karkus P, Xu D, et al (2024a) Storm: Spatio-temporal reconstruction model for large-scale outdoor scenes. arXiv preprint arXiv:250100602 2, 4, 10, 11, 12, 13, 3

Yang Z, Chen Y, Wang J, Manivasagam S, Ma WC, Yang AJ, Urtasun R (2023b) Unisim: A neural closed-loop sensor simulator. In: Proceedings of the IEEE/CVF Conference on Computer Vision and Pattern Recognition, pp 1389–1399 1, 3

Yang Z, Gao X, Zhou W, Jiao S, Zhang Y, Jin X (2024b) Deformable 3d gaussians for high-fidelity monocular dynamic scene reconstruction. In: Proceedings of the IEEE/CVF conference on computer vision and pattern recognition, pp 20331–20341 18

Ye C, Nie Y, Chang J, Chen Y, Zhi Y, Han X (2024a) Gaustudio: A modular framework for 3d gaussian splatting and beyond. arXiv preprint arXiv:240319632 1, 8

Ye V, Li R, Kerr J, Turkulainen M, Yi B, Pan Z, Seiskari O, Ye J, Hu J, Tancik M, Kanazawa A (2024b) gsplat: An open-source library for Gaussian splatting. arXiv preprint arXiv:240906765 URL <https://arxiv.org/abs/2409.06765>, 2409.06765 9

Yin W, Zhang C, Chen H, Cai Z, Yu G, Wang K, Chen X, Shen C (2023) Metric3d: Towards zero-shot metric 3d prediction from a single image. In: Proceedings of the IEEE/CVF International Conference on Computer Vision, pp 9043–9053 16

Yu A, Ye V, Tancik M, Kanazawa A (2021) pixelnerf: Neural radiance fields from one or few images. In:

Proceedings of the IEEE/CVF Conference on Computer Vision and Pattern Recognition, pp 4578–4587

4

Yu H, Lin H, Wang J, Li J, Wang Y, Zhang X, Wang Y, Zhou X, Hu R, Peng S (2026) Infinidepth: Arbitrary-resolution and fine-grained depth estimation with neural implicit fields. arXiv preprint arXiv:260103252

18

Zhang C, Zou Y, Li Z, Yi M, Wang H (2024a) Transplat: Generalizable 3d gaussian splatting from sparse multi-view images with transformers. arXiv preprint arXiv:240813770

4

Zhang J, Herrmann C, Hur J, Jampani V, Darrell T, Cole F, Sun D, Yang MH (2024b) Monst3r: A simple approach for estimating geometry in the presence of motion. arXiv preprint arXiv:241003825

4

Zhang K, Bi S, Tan H, Xiangli Y, Zhao N, Sunkavalli K, Xu Z (2025a) Gs-lrm: Large reconstruction model for 3d gaussian splatting. In: European Conference on Computer Vision, Springer, pp 1–19

4

Zhang S, Wang J, Xu Y, Xue N, Rupprecht C, Zhou X, Shen Y, Wetzstein G (2025b) Flare: Feed-forward geometry, appearance and camera estimation from uncalibrated sparse views. 2025 IEEE/CVF Conference on Computer Vision and Pattern Recognition (CVPR) pp 21936–21947, URL <https://api.semanticscholar.org/CorpusID:276422283>

4

Zhou H, Shao J, Xu L, Bai D, Qiu W, Liu B, Wang Y, Geiger A, Liao Y (2024a) Hugs: Holistic urban 3d scene understanding via gaussian splatting. In: Proceedings of the IEEE/CVF Conference on Computer Vision and Pattern Recognition, pp 21336–21345

3

Zhou QY, Park J, Koltun V (2018) Open3d: A modern library for 3d data processing. arXiv preprint arXiv:180109847

1

Zhou X, Lin Z, Shan X, Wang Y, Sun D, Yang MH (2024b) Drivinggaussian: Composite gaussian splatting for surrounding dynamic autonomous driving scenes. In: Proceedings of the IEEE/CVF Conference on Computer Vision and Pattern Recognition, pp 21634–21643

3

Supplementary Material for: EVolSplat4D: Efficient Volume-based Gaussian Splatting for 4D Urban Scene Synthesis

S1 Analysis of the convergence of $\Delta\mu_i$

In this section, we will show the position offset $\Delta\mu_i$ converges to a fixed value at the infinite training iterations. Recall that the $\Delta\mu_i$ in the iteration k can be formulated as:

$$\mathbf{h}_i = \mathcal{V}(\mu_i^{init} + \Delta\mu_i^{k-1}) \quad (S1)$$

$$\Delta\mu_i^k = \text{Tanh}(\mathcal{D}_{cr}^{pos}(\mathbf{h}_i)) \cdot v_{size} \quad (S2)$$

We can derive the $\Delta\mu_i^k$ as:

$$\Delta\mu_i^k = \text{Tanh}(\mathcal{D}_{cr}^{pos}(\mathcal{V}(\mu_i^{init} + \Delta\mu_i^{k-1}))) \cdot v_{size} \quad (S3)$$

We define $\mathcal{H} \triangleq \text{Tanh}(\mathcal{D}_{cr}^{pos}(\mathcal{V}(\cdot))) \cdot v_{size}$ for simplicity, i.e.,

$$\Delta\mu_i^k = \mathcal{H}(\mu_i^{init} + \Delta\mu_i^{k-1}) \quad (S4)$$

Given that $\Delta\mu_i$ small, we apply the first-order Taylor expansion to approximate Eq. S4:

$$\Delta\mu_i^k = \mathcal{H}(\mu_i^{init}) + \left. \frac{\partial \mathcal{H}}{\partial \mu} \right|_{\mu_i^{init}} \Delta\mu_i^{k-1} \quad (S5)$$

Considering that $\beta \triangleq \mathcal{H}(\mu_i^{init})$ and $\Gamma \triangleq \left. \frac{\partial \mathcal{H}}{\partial \mu} \right|_{\mu_i^{init}}$ are both constants, we reformulate Eq. S5 as:

$$\Delta\mu_i^k = \beta + \Gamma \Delta\mu_i^{k-1} \quad (S6)$$

The training converges in our experimental observations. Therefore, we assume $\Delta\mu_i^\infty$ converges as k approaches the infinite step, i.e., $k \rightarrow \infty$. This allows us to derive $\Delta\mu_i^\infty$:

$$\Delta\mu_i^\infty = \beta + \Gamma \Delta\mu_i^\infty \quad (S7)$$

$$= (\mathbf{I} - \Gamma)^{-1} \beta \quad (S8)$$

This indicates that μ_i^∞ converges to a constant value. In the main paper Table 7, we show that μ_i^t converges quickly at early steps during inference.

S2 Implementation Details

S2.1 Remove Depth Outliers

We begin by applying a depth consistency check to filter out noisy depth data. Specifically, we unproject the depth map D_i of i th frame to 3D and reproject it to a nearby view j , obtaining a projected depth $D_{i \rightarrow j}$. Next, we compare $D_{i \rightarrow j}$ and D_j and filter out depths where the absolute relative error exceeds an empirical threshold $\sigma = 0.2m$. We formulate this process as:

$$M_d = |D_{i \rightarrow j} - D_j| < \sigma, D_{i \rightarrow j} = D_j (\pi_j \pi_i^{-1}(\mathbf{u}_i)) \quad (S9)$$

where \mathbf{u}_i denotes pixel coordinates of i th frame and M_d represents the geometric consistency mask. We further utilize the 3D statistical filter in Open3D Zhou et al (2018) to remove the clear floaters in the unprojected point clouds for each frame. In our implementation, we set the number of neighbors to 20 and the standard deviation ratio to 2.0.

S2.2 Close-Range Gaussian Prediction Details

Following Kerbl et al (2023), Σ is decomposed into two learnable components: rotation matrix \mathbf{R} and a scaling matrix \mathbf{S} to hold practical physical significance, see the following formula:

$$\Sigma = \mathbf{R} \mathbf{S} \mathbf{S}^T \mathbf{R}^T \quad (S10)$$

To allow independent optimization of both factors, we use a 3D vector s representing scaling and a quaternion q for rotation separately. Instead of directly learning scales s , we initialize the s_{init} with the average distance of K nearest neighbors using the KNN algorithm and learn the scales residual Δs from the volume latent feature \mathbf{h}_i via a decoder \mathcal{D}_{cr}^{cov} . We experimentally observe that the residual learning strategy helps our network converge faster and enhances the model capacity.

$$\mathbf{s} = \mathbf{s}_{init} + \Delta s, \quad \Delta s = \mathcal{D}_{cr}^{cov}(\mathbf{h}_i) \quad (S11)$$

S2.3 SparseCNN Network Architecture

We build a generalizable efficient 3DCNN \mathcal{F}^{3D} to provide the geometric priors for the foreground contents. Given the global neural point cloud $\mathcal{P} \in \mathbb{R}^{N_p \times 16}$, we quantize the point cloud with the voxel size $v_{\text{size}} = 0.1m$ and feed these sparse tensors into the \mathcal{F}^{3D} to predict the latent feature volume \mathcal{V} . The sparse 3DCNN uses a U-Net like architecture with skip connections, comprising some convolution and transposed convolution layers. The details of 3DCNN are listed in the Tab. S1. We use torchsparse as the implementation of \mathcal{F}^{3D} .

SparseCNN Network Architecture

Layer	Description	In/Out Ch.
Conv ₀	kernel = $3 \times 3 \times 3$, stride = 1	16/16
Conv ₁	kernel = $3 \times 3 \times 3$, stride = 2	16/16
Conv ₂	kernel = $3 \times 3 \times 3$, stride = 2	16/32
Conv ₃	kernel = $3 \times 3 \times 3$, stride = 1	32/32
Conv ₄	kernel = $3 \times 3 \times 3$, stride = 2	32/64
Conv ₅	kernel = $3 \times 3 \times 3$, stride = 1	64/64
DeConv ₆	kernel = $3 \times 3 \times 3$, stride = 2	64/32
DeConv ₇	kernel = $3 \times 3 \times 3$, stride = 2	32/32
DeConv ₈	kernel = $3 \times 3 \times 3$, stride = 2	32/16
DeConv ₉	kernel = $3 \times 3 \times 3$, stride = 2	16/16

Table S1: **Architecture of SparseConvNet.** Each layer consists of sparse convolution, batch normalization, and ReLU.

S3 Datasets

We conduct experiments on four autonomous driving datasets: KITTI-360 [Liao et al \(2022\)](#), KITTI [Geiger et al \(2013\)](#), Waymo Open Dataset [Sun et al \(2020\)](#) and PandaSet [Xiao et al \(2021\)](#).

KITTI-360: We use the KITTI-360 dataset [Liao et al \(2022\)](#) for pre-training our static scenes. The training set consists of 160 static clips from sequences 00, 02, and 04, using both the front two stereo cameras. For static experiments, we follow the Drop 50% protocol of KITTI-360. To be specific, we define a stereo image pair (left and right camera) as the base unit and select only the odd-numbered pairs ($\text{id}=0 2 4 6 \dots$) for training. The test frames are selected as the left-eye image of even-numbered pairs ($\text{id}=1 3 5 7 \dots$) to avoid overlapping with the training frames.

Waymo: The Waymo Open Dataset is collected from various locations across the United States, containing

a rich mix of static and dynamic scenes. In our feed-forward experiment for static scenes, the Waymo dataset is not used for training but serves as an out-of-domain dataset to evaluate our model’s zero-shot generalization. In the dynamic feed-forward experiment, we follow the 80% drop rate as in STORM [Yang et al \(2024a\)](#) experimental setup for a fair comparison. To be specific, every 5th frame ($\text{id}=0 5 10 15 \dots$) is selected as the training frame, while the remaining frames are used for testing. For comparison with per-scene optimization baselines, we maintain the 80% drop rate to simulate sparse inputs.

KITTI: To comprise more dynamic scenes, we augment our model with clips from the KITTI dataset. We select five clips to evaluate the model generalization capacity. Same as other dataset, the testsets from KITTI have no overlap with the training sets. Moreover, we follow the MARS [Wu et al \(2023\)](#) using sequence 01 and 06 to demonstrate our model’s capability for scene editing.

PandaSet: PandaSet [Xiao et al \(2021\)](#) serves as our primary out-of-domain dataset for dynamic feed-forward reconstruction. Our model is never trained on PandaSet, but we select five representative sequences to evaluate its zero-shot generalization performance.

S4 Baselines

In this section, we discuss the state-of-the-art baselines used for comparison with our approach. All experiments are conducted on NVIDIA RTX 5880, except PixelSplat, MVSplat, and STORM are trained on NVIDIA V100 since their transformer-based architecture requires a large amount of GPU memory.

Feed-Forward Static Baselines: Our static baselines include two categories: **NeRF-based methods** (MVSNeRF [Chen et al \(2021\)](#), MURF [Xu et al \(2023\)](#), and EDUS [Miao et al \(2024\)](#)) and **3DGS-based methods** (PixelSplat [Charatan et al \(2024\)](#), MVSplat [Chen et al \(2024b\)](#), DepthSplat [Xu et al \(2025\)](#), EVolSplat [Miao et al \(2025\)](#)) and AnySplat [Jiang et al \(2025a\)](#). For a fair comparison, we adopt the official implementations and default settings for all baselines but retrain them from scratch on our static dataset under the Drop50% setting.

For NeRF-based baselines, MVSNeRF and MuRF utilize multi-view stereo (MVS) algorithms to construct the cost volume and apply 3DCNN to reconstruct a neural field while EDUS leverages the depth priors to learn a generalizable scene representation. For 3DGS-based baselines, PixelSplat predicts 3D Gaussians with

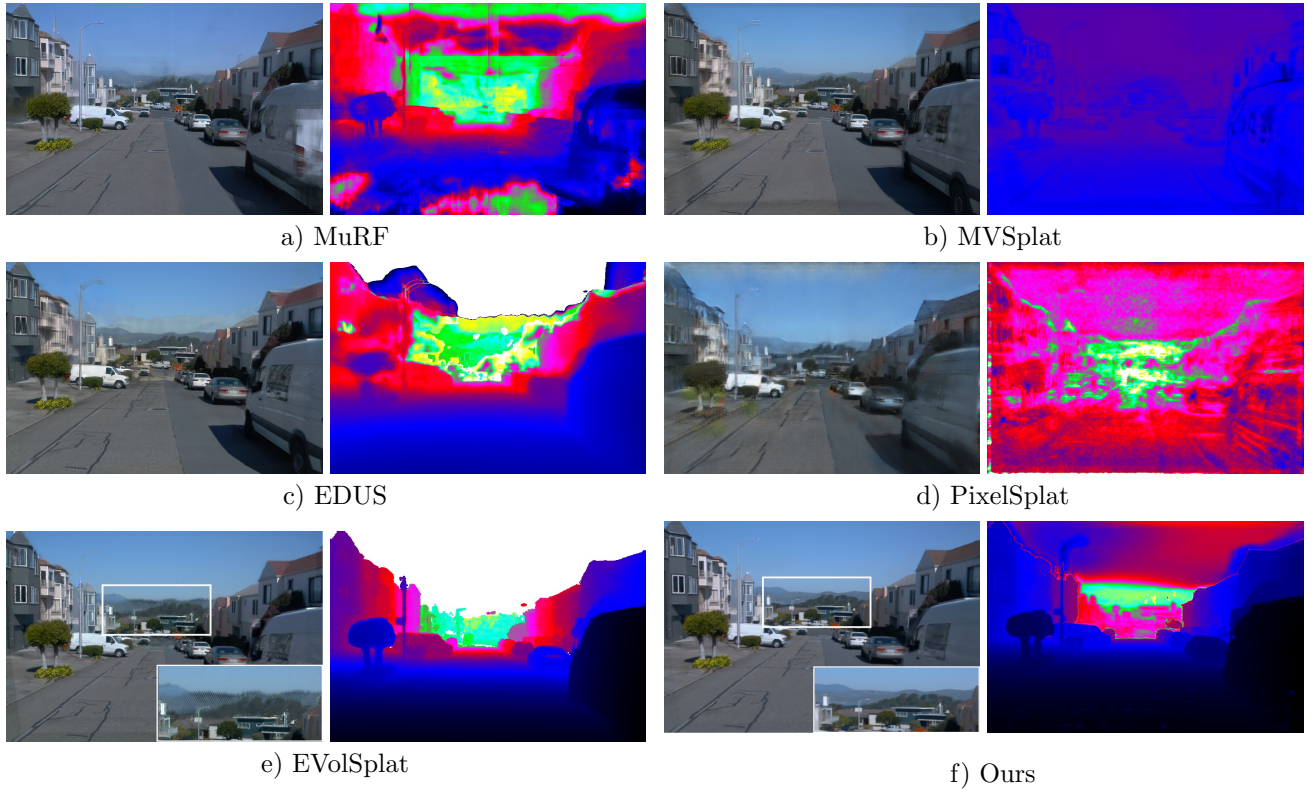


Fig. S1: **Qualitative Comparisons** with baselines for zero-shot inference on the Waymo static scenes. Better to zoom in for the far-field scenery improvements.

a two-view epipolar transformer and then spawns per-pixel Gaussians. MVsplat exploits multi-view correspondence information for geometry learning and predicts 3D Gaussians from image features. Built on MVsplat, DepthSplat further leverages pre-trained monocular depth features to enhance model capacity. AnySplat distills geometry priors from powerful VGGT Wang et al (2025b) and employs a geometry transformer to directly decode Gaussian parameters and camera poses from images. While EVolSplat achieves on-par results on KITTI-360, its simple hemisphere background struggles to model the complex, fine-grained far-range landscapes in the Waymo dataset. This limitation directly motivates the design of our new **Generalizable Far-Field Branch**, which is introduced in the main paper.

Feed-Forward Dynamic Baselines: We compare against two state-of-the-art dynamic baselines, DrivingRecon Lu et al (2024) and STORM Yang et al (2024a), as well as our static-only conference version, EVolSplat Miao et al (2025). This comparison demonstrates that our new version can effectively handle dynamic environments. We adopt the official implementations and default setting for all baselines, training and evaluating them under the Drop80% setting.

DrivingRecon is a pioneering method for generalizable dynamic reconstruction from surround-view inputs. It utilizes an encoder-decoder model with temporal cross-attention to predict 4D Gaussians directly. The latest work STORM (ICLR 2025), uses a data-driven Transformer architecture to predict per-pixel Gaussian attributes and additional velocity in a self-supervised manner. These independent Gaussians can then be warped to any particular timestamp using the velocity estimates to perform novel view rendering.

Per-Scene Optimization-based Baseline: To evaluate how our generalizable priors help improve reconstruction quality from sparse inputs, we compare them against the recent per-scene optimization methods for autonomous driving scenarios under 80% drop rate, including SUDS Turki et al (2023), EmerNeRF Yang et al (2023a), StreetGaussian Yan et al (2024), DeSiRe-GS Peng et al (2025) and OmniRe Wei et al (2025).

SUDS and EmerNeRF capture scene appearance, motion, and semantic features by decomposing scenes into static and dynamic fields, learning a flow field to represent a 4D neural radiance field. StreetGaussian and OmniRe leverage ground-truth 3D bounding boxes to decompose static background and dynamic elements. They model each dynamic actor with a dedicated local

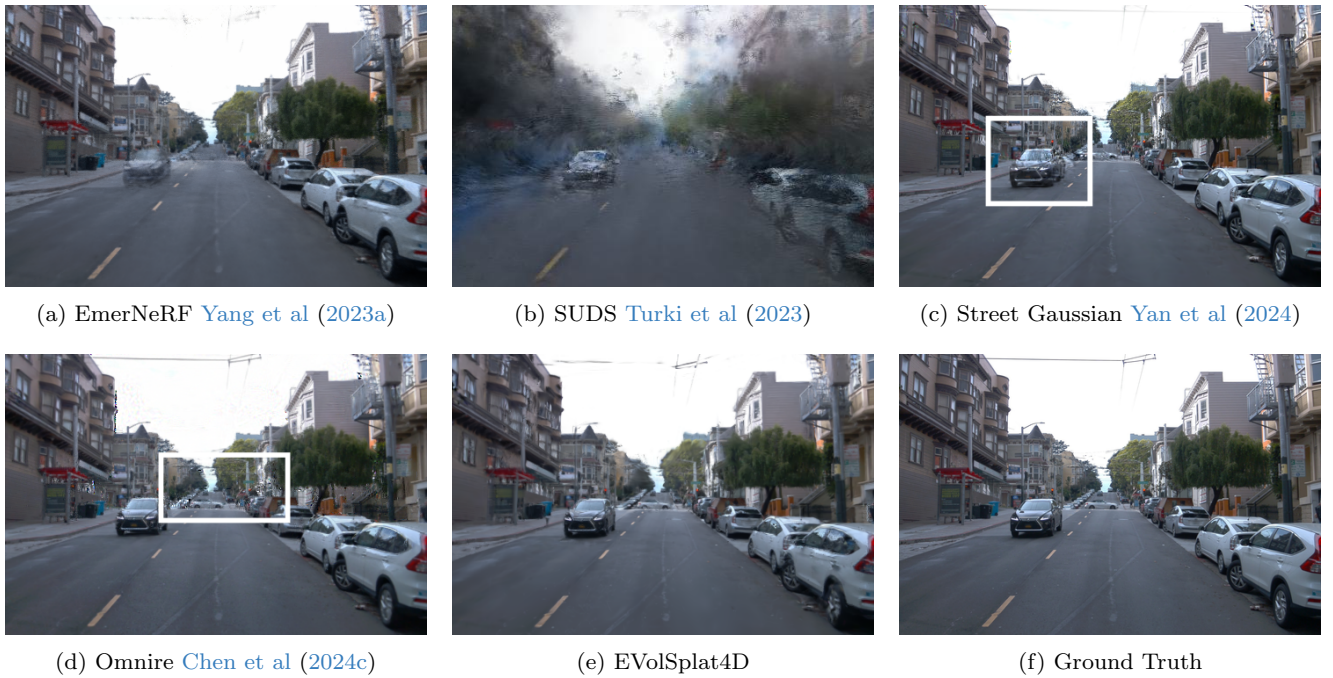


Fig. S2: **Qualitative scene reconstruction comparisons** with per-scene optimization baselines under the Drop80% sparsity level

canonical space based on the Gaussian Splatting representation, showing impressive reconstruction ability. DeSiRe-GS adopts a two-stage pipeline to first extract 2D motion masks from the feature difference between the rendered and supervision images, and then distill this 2D motion information into Gaussian space.

S5.2 Qualitative Comparison with Optimization-based Methods

We present qualitative comparisons in Fig. S2 under the Drop80% setting. The quantitative results are reported in the main paper. Our method achieves superior performance against all baselines, which we attribute to the robust, generalizable priors.

S5 Additional Experimental Results

S5.1 More Static Feed-Forward Qualitative results

We provide more qualitative results on the Waymo dataset via a feed-forward inference on the static scenes. MuRF Xu et al (2023) achieves promising rendering results on Waymo, but it struggles with poor geometric reconstruction in texture-less areas, such as roads, due to its strong reliance on feature mapping. To better present the improvements in the far-range regions, we provide zoomed-in comparisons in Fig. S1. EVolSplat Miao et al (2025), despite achieving high-quality rendering in the close range, presents clear artifacts in the background region due to its coarse hemisphere background model. In contrast, our Generalizable Far-Field Branch effectively models the complex, fine-grained distant landscapes, overcoming the limitations of prior work.

S5.3 More Dynamic Feed-Forward Qualitative results

Our method enables efficient dynamic reconstruction and real-time photorealistic NVS from flexible sparse street view images. We provide more qualitative dynamic reconstruction results on three different datasets (KITTI, Waymo and PandaSet) as shown in Fig. S5, Fig. S3 and Fig. S4.



Fig. S3: **More Qualitative Results on Waymo.** We visualize synthesized images (odd rows) and the corresponding predicted dynamic actors (even rows) on novel scenes generated by our pretrained model through a feed-forward inference.

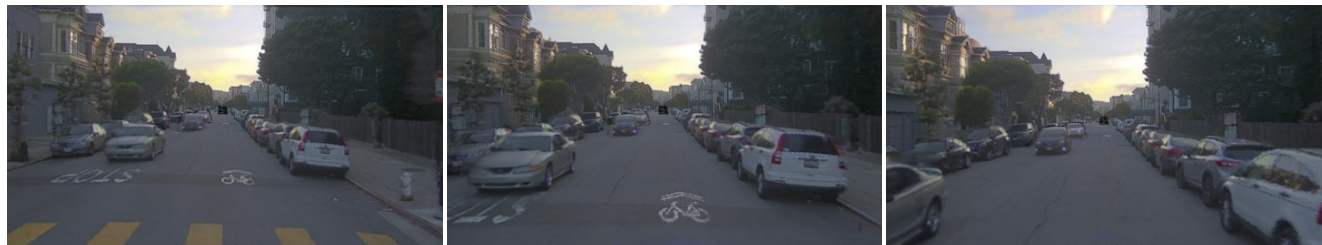


Fig. S4: **More Qualitative Results on out-of-domain dataset PandaSet.** We visualize synthesized images (odd rows) and the corresponding predicted dynamic actors (even rows) on novel scenes generated by our pretrained model through a feed-forward inference.



Fig. S5: **More Qualitative Results on KITTI.** We visualize synthesized images (odd rows) and the corresponding predicted dynamic actors (even rows) on novel scenes generated by our pretrained model through a feed-forward inference.